Deng, K., Wittmann, H., von Blanckenburg, F. (2020):
The depositional flux of meteoric cosmogenic 10Be
from modeling and observation. - Earth and
Planetary Science Letters, 550, 116530.

https://doi.org/10.1016/j.epsl.2020.116530

The depositional flux of meteoric cosmogenic ^{10}Be from modeling and observation

Kai Deng[a,b], Hella Wittmann[a], Friedhelm von Blanckenburg[a,c]

[a] *GFZ German Research Centre for Geosciences, Earth Surface Geochemistry, Telegrafenberg, 14473 Potsdam, Germany*

[b] *State Key Laboratory of Marine Geology, Tongji University, 200092 Shanghai, China*

[c] *Institute of Geological Sciences, Freie Universität Berlin, 12249 Berlin, Germany*

**Corresponding author:*

Kai Deng

E-mail: 103459@tongji.edu.cn

Abstract: Meteoric cosmogenic ^{10}Be is a powerful tracer to quantify dates and rates of Earth surface processes over timescales of 10^3-10^5 yrs. A prerequisite for its applications is knowledge of the flux at which ^{10}Be, produced in the atmosphere, is delivered to the Earth surface. Four entirely independent approaches are available to quantify this flux: 1) General Circulation Models (GCM) combined with ^{10}Be production functions and aerosol dynamics; 2) ^{10}Be in precipitation collections; 3) ^{10}Be inventories in dated soil profiles; 4) riverine ^{10}Be exported in solid and dissolved forms. We compiled and reprocessed published globally distributed ^{10}Be flux data from each of these methods and compared them with each other after normalization to a common atmospheric production rate. Based on precipitation records, we propose a simple framework to discriminate between two delivery effects on ^{10}Be fluxes. In the additive effect water vapor and ^{10}Be are continuously accumulating during long-distance transport, leading to an increase in ^{10}Be flux with precipitation rate. In the dilution effect, the ^{10}Be flux is delivered from proximal vapor sources, limited by the rate of ^{10}Be introduction from the stratosphere and independent of precipitation rate. Both effects are mostly present in combination, and the relative weight of either effect depends on vapor condensation rate and on the ratio of vapor condensation area to precipitation area. A comparison between precipitation-derived fluxes and GCM-derived fluxes shows that half of the precipitation estimates are >2 times greater than GCM-derived fluxes. By comparison, soil- and GCM-derived fluxes agree within a factor of 2 for more than half (~57%) of the dataset, and the remaining soil estimates (~43%) are much lower than GCM-derived fluxes. 71% of ^{10}Be flux estimates from riverine export using ^{10}Be (meteoric)/^{9}Be ratios also agree with GCM-derived fluxes within a factor of 2. We explain the precipitation-derived fluxes that commonly exceed all other estimates by short-term stochasticity in precipitation events that might introduce a measurement time-interval bias towards higher fluxes. This bias is not present over longer-term (10^3-10^5 yrs) flux estimates like those from soil profiles. Soil-derived fluxes might still present an underestimation when retention of ^{10}Be in soil is incomplete. We recommend producing more ^{10}Be depositional flux data from soil inventories with full Be retention, as these generate in our view the most relevant estimates for applications of meteoric ^{10}Be on millennial-scale Earth surface processes.

Keywords: cosmogenic nuclides, meteoric ^{10}Be, general circulation model (GCM), production rates, Earth surface processes, geochronology

1. Introduction

When galactic cosmic rays impinge upon the atmosphere, they induce spallation reactions in oxygen and nitrogen atoms that produce meteoric cosmogenic nuclide beryllium-10 (^{10}Be) that is radioactive with a half-life of 1.39 Myr (Chmeleff et al., 2010). Meteoric ^{10}Be is scavenged from the atmosphere primarily by precipitation after adhering to aerosols. When delivered to the Earth's surface it binds tightly to soil particles provided that the pH of soil solutions is circum-neutral. The concentration of meteoric ^{10}Be measured in Earth surface materials is thus controlled by the following processes: ^{10}Be production and redistribution in the atmosphere, ^{10}Be delivery to the surface, ^{10}Be retention in the substrate, and substrate stability with regards to erosion (Willenbring and von Blanckenburg, 2010b). As such, meteoric ^{10}Be has been used as a tracer for a wide range of Earth surface processes over timescales of 10^3-10^5 yrs, including determining soil residence time (Bacon et al., 2012; Pavich et al., 1986) and ages of sediment archives (Egli et al., 2010; Lebatard et al., 2010), tracing soil movement (Jungers et al., 2009; Mckean et al., 1993), quantifying rates of erosion and weathering over hillslope scale (Maher and von Blanckenburg, 2016) and over basin scale (Brown et al., 1988; Portenga et al., 2019; von Blanckenburg et al., 2012; Wittmann et al., 2015), and also the expression of these processes back through time (von Blanckenburg et al., 2015; Willenbring and von Blanckenburg, 2010a). In order to quantify these dates and rates of Earth surface processes using meteoric ^{10}Be, knowledge of the ^{10}Be depositional flux is a key prerequisite.

^{10}Be production in the atmosphere depends on the primary cosmic ray flux and thus on solar activity and geomagnetic field strength (Masarik and Beer, 2009). After production, ^{10}Be is well-mixed in the stratosphere (~1 yr) and hydrolyzed to surface-reactive $Be(OH)_2$. After adsorption to atmospheric aerosols, ^{10}Be is delivered to Earth's surface by wet and dry deposition. The delivery thus depends on

atmospheric aerosol loading and climate, which can significantly modify the temporal and spatial distribution of ^{10}Be depositional fluxes (Field et al., 2006; Heikkilä et al., 2013b). Over recent decades, substantial efforts on modeling and observation have been conducted to advance our knowledge of ^{10}Be deposition over a range of temporal and spatial scales. These efforts include four independent approaches.

1) Atmospheric production and delivery models (Heikkilä et al., 2013a). In order to study production, atmospheric transport and deposition of meteoric ^{10}Be, physics-based ^{10}Be production functions (Masarik and Beer, 2009) and aerosol physics-chemistry (Stier et al., 2005) have been coupled with atmospheric general circulation models (GCM) (Schmidt et al., 2006; Stier et al., 2005). These integrated models have revealed the spatio-temporal pattern of ^{10}Be depositional flux and its response to variations in solar activity, geomagnetic field strength (Field et al., 2006; Heikkilä et al., 2008b), and climate, including atmospheric mixing and precipitation (Heikkilä et al., 2013b; Heikkilä and Smith, 2013).

2) Precipitation collections. Over contemporary timescales, ^{10}Be measurements in rainfall and snow in combination with precipitation rates yield local depositional fluxes. Based on such data, previous studies investigated the effects of latitude (Graly et al., 2011), altitude (Heikkilä et al., 2008a), stratosphere-troposphere exchange (Graham et al., 2003), precipitation rate (Willenbring and von Blanckenburg, 2010b), and aerosol content (Mann et al., 2011) on ^{10}Be depositional fluxes.

3) Soil profiles. Over millennial timescales, inventories of meteoric ^{10}Be in non-eroding soil profiles of known ages, developed on river terraces, moraine deposits, or bedrock, provide site-specific depositional fluxes that average over 10^3 to 10^5 years when assuming full retention (Dixon et al., 2018; Ouimet et al., 2015; Reusser et al., 2010). If ^{10}Be retention is incomplete in soil profiles, this approach provides a lower-limit estimate (Maher and von Blanckenburg, 2016; Schoonejans et al., 2017).

4) Riverine fluxes. Over erosion and weathering timescales (e.g. 10^3-10^4 yrs), the atmospheric input flux of ^{10}Be is expected to be balanced by the riverine sedimentary and dissolved ^{10}Be flux (Wittmann et

al., 2015). Assuming such steady state, the ^{10}Be flux from riverine export thus reflects the ^{10}Be depositional flux over this long timescale.

Previous studies, including Willenbring and von Blanckenburg (2010b) and Graly et al. (2011), investigated the fluxes derived from different approaches by comparing modeled with measured ^{10}Be depositional fluxes on the one hand, and short-term (precipitation-derived) with long-term (soil-derived) ^{10}Be depositional fluxes in the other hand, respectively. In both types of comparison, the overall agreement between approaches was encouraging. However, in recent studies (Dixon et al., 2018; Ouimet et al., 2015), the ^{10}Be depositional fluxes obtained from dated soil profiles clearly differed from flux estimates by GCM (Heikkilä and von Blanckenburg, 2015), and also from a fitting equation based on precipitation ^{10}Be records (Graly et al., 2011). The lack of agreement between these estimates has been explained by local climatic variability (Heikkilä et al., 2013a), lack of suitability of soil inventories, or failure to adequately account for temporal variations in cosmic ray fluxes.

An understanding of the climatic control on ^{10}Be depositional flux, meaning the relationship between ^{10}Be concentration, flux, and precipitation rate, is essential for upscaling contemporary ^{10}Be fluxes in space and time. In this regard, two contrasting views exist. One observation holds that the ^{10}Be depositional flux is positively correlated with precipitation rate, and that this precipitation dependence can explain the variations of ^{10}Be inventories in some soil profiles (Dixon et al., 2018; Graly et al., 2011). Other studies show no correlation between ^{10}Be flux and precipitation, and regard the ^{10}Be flux to be independent of precipitation (Ouimet et al., 2015; Willenbring and von Blanckenburg, 2010b). To account for these disparate views, Willenbring and von Blanckenburg (2010b) proposed two ^{10}Be delivery effects: the “dilution effect” and the “additive effect”. In the dilution effect, precipitation is delivered from moist air mass with proximal vapor sources where moisture has high turnover rates, such that the delivery of meteoric ^{10}Be is ultimately limited by the rate at which it is introduced into moist air mass by stratospheric production. Hence the ^{10}Be concentration in precipitation can be “diluted” (Willenbring and von Blanckenburg, 2010b). In the additive effect, water vapor is continuously accumulating in moist air

112 mass during long-distance transport, and so is ^{10}Be, such that the ^{10}Be depositional flux will increase with
113 precipitation rate (Graly et al., 2011). However, the competition between both effects is still unclear and
114 requires a comprehensive comparison between flux estimates across spatial and temporal scales.

115 In this study, we compiled literature data and recalculated ^{10}Be fluxes recorded in different kinds of
116 materials including precipitation, soil profiles and riverine solid and solute loads, and compared them to
117 modeled (GCM-derived) ^{10}Be depositional fluxes given the wide spatial coverage (i.e. global scale) of the
118 GCM-derived dataset. The main aim is to evaluate the reliability of ^{10}Be depositional fluxes from each
119 approach and the associated bias in flux derivation. This study advances the understanding of meteoric
120 ^{10}Be delivery and deposition over a range of spatial and temporal scales, and provides new insights on
121 method-specific uncertainties on ^{10}Be flux estimates which shall benefit future Earth surface applications
122 using meteoric ^{10}Be.

123 **2. Methods: compilation of modeled and measured ^{10}Be fluxes and assessment of delivery effects**

124 *2.1. GCMs with ^{10}Be production functions and aerosol dynamics*

125 To investigate the spatio-temporal pattern of ^{10}Be deposition, two GCMs, including GISS (Goddard
126 Institute for Space Studies) ModelE (Field et al., 2006) and ECHAM5 (European Centre for Medium-
127 Range Weather Forecasts-Hamburg Model 5)-HAM (Heikkilä et al., 2013a), were previously applied by
128 incorporating meteoric ^{10}Be production functions in the atmosphere (Masarik and Beer, 2009) and aerosol
129 physics-chemistry. Comparing both models, the GISS ModelE with 20 vertical layers and a horizontal
130 resolution of 4°×5° (Field et al., 2006) shows a coarser spatial resolution than the ECHAM5-HAM that
131 includes 31-39 vertical layers and a horizontal resolution of 2.8°×2.8° (Heikkilä et al., 2008b). It has been
132 suggested (Heikkilä et al., 2013a) that the lower spatial resolution of GISS ModelE (Field et al., 2006)
133 might bias the modeling of atmospheric mixing and advection of ^{10}Be, leading to artificial latitudinal
134 differences in the response of ^{10}Be deposition to production changes (Heikkilä et al., 2008b). We thus
135 focus on the modeled ^{10}Be depositional flux derived from the ECHAM5-HAM (Fig. 1).

We used published results of the ECHAM5-HAM model based on a ^{10}Be production rate calculated for a modern solar modulation factor (ϕ in MeV) of 501.76 MeV (Fig. 2). To account for the climate-related uncertainty introduced by spatial variations in ^{10}Be delivery over the Holocene, we used two different model outputs: one for modern ("industrial", time span: 1977-2006) climatic conditions (Heikkilä and Smith, 2013) and the other for the early Holocene ("pre-industrial", time span: 12-10 kyr BP) conditions (Heikkilä et al., 2013b). The difference in the spatial pattern of modeled ^{10}Be depositional fluxes between both runs is our estimate of flux uncertainty (Heikkilä and von Blanckenburg, 2015). Here, the modeled fluxes of both runs under modern production conditions were rescaled to the average Holocene ^{10}Be production rate (Fig. 2). The resulting distribution map (Fig. 1) shows the average flux of both rescaled model runs.

2.2. Precipitation collections

We compiled ^{10}Be data from precipitation collectors ($[^{10}Be]_{rain}$, in at/m^3) and the corresponding precipitation rate (P, in m^3/m^2/yr)) to calculate the ^{10}Be depositional flux (F_{met}, in at/m^2/yr)):

$$F_{met}=[^{10}Be]_{rain}\times P \quad (1)$$

The analytical uncertainty of $[^{10}Be]_{rain}$ was propagated into the uncertainty of F_{met}. To obtain an annual ^{10}Be depositional flux from measured monthly data, we calculated the monthly-precipitation-weighted ^{10}Be concentration and multiplied it by the annual precipitation rate. The derived flux is the sum of three components: wet deposition (scavenging of $^{10}Be(OH)_2$ by precipitation), dry deposition (delivery by friction-based aerosol deposition), and the recycled fraction (^{10}Be carried by dust). This precipitation dataset covers continental settings (Fig. 1), including Switzerland (Heikkilä et al., 2008a), India (Somayajulu et al., 1984), and USA (Monaghan et al., 1986), and islandic settings, including Trinidad (Brown et al., 1992), Kikai Island (Japan) (Maejima et al., 2005) and New Zealand (Graham et al., 2003). Records with an observation period <9 months (see details in Supplementary dataset) are considered unrepresentative over the annual scale as they might be biased by seasonal cycles (Heikkilä and Smith,

160 2013), and thus these ^{10}Be data are shown in figures for completeness but excluded from the discussion of
161 fluxes.

162 We applied normalization procedures that account for variations in the flux of galactic cosmic rays
163 and analytical differences, to compare between datasets of different observation periods and derived from
164 different methods (Fig. 2). 1) All ^{10}Be concentrations were normalized to the AMS (accelerator mass
165 spectrometry) standard KNSTD07 (Nishiizumi et al., 2007). 2) Precipitation records that are subject to
166 inter-annual variations in solar modulation were normalized to a common modern solar modulation factor
167 of 501.76 MeV. 3) The contemporary precipitation-derived fluxes were further normalized to the average
168 Holocene ^{10}Be production rate by multiplying them with ~1.23 which is the ratio of Holocene relative to
169 modern production and encompasses variations in solar modulation and magnetic field strength
170 (Steinhilber et al., 2012) (Fig. 2).

171 *2.3. Soil profiles*

172 Over a timescale integrated by most geomorphic processes (10^3-10^5 yrs), the site-specific ^{10}Be
173 depositional flux can be calculated from the total ^{10}Be inventory (at/m^2) measured in soil profiles.
174 Prerequisites are a known age of the onset of soil formation (t, in yr) and full retention of meteoric ^{10}Be.
175 In the case of an alluvial substrate any meteoric ^{10}Be ($[^{10}Be]_{inh}$, in at/kg) inherited prior to deposition that
176 is apparent at the bottom of profiles should be subtracted. The equation for calculating F_{met} as modified
177 from Egli et al. (2010) is:

178 $$F_{met} = \sum_{i=1}^{n} \left[\left([^{10}Be]_{s,i} - [^{10}Be]_{inh,i} \right) \times \rho_i \times z_i \times V_{f,i} \right] \times \lambda / (1 - e^{-\lambda t}) \quad (2)$$

179 where $[^{10}Be]_{s,i}$ is the soil ^{10}Be concentration (at/kg) at ith horizon, ρ_i the soil bulk density (kg/m^3), z_i
180 the thickness of the ith horizon (m), $V_{f,i}$ the volume percentage (%) of the fine earth fraction (<2 mm)
181 containing ^{10}Be at the ith horizon, λ the decay constant of ^{10}Be (5×10^{-7} yr^{-1}). If no V_f data was reported in
182 literature because the fine fraction dominates, V_f of 100% is used. The uncertainty of the resulting F_{met} is
183 propagated from the individual uncertainties of the ^{10}Be measurement, the age determination, 10% for soil

density measurements, and 5% for V_f (Egli et al., 2010). We compiled ^{10}Be data from soil profiles (Fig. 1) located in continental settings, including European Alps (Egli et al., 2010) and the USA (Balco, 2004; Ouimet et al., 2015), and in islandic settings, including Hawaii (Dixon et al., 2018) and New Zealand (Reusser et al., 2010). We did not compile or show data from other archives like coral reefs (Maejima et al., 2005) or old soil profiles (age >200 ka) (Pavich et al., 1986) here because of ^{10}Be contamination by seawater and a high potential for surface erosion and incomplete retention, respectively. We applied 1) the AMS normalization same as above and 2) a millennial-scale variability normalization, depending on the integration timescale of each soil profile, to the average Holocene ^{10}Be production rate for comparison with other approaches (Fig. 2).

Some of the compiled profiles are considered to be affected by significant erosional loss, sampling depth not sufficient to quantify the ^{10}Be inheritance, or excessive ^{10}Be inheritance. These are shown in figures for completeness but excluded from the discussion of fluxes (see details in Supplementary dataset).

2.4. Riverine export

Over the river basin scale, when assuming steady state of ^{10}Be fluxes over weathering and erosion timescales, the basin-averaged ^{10}Be depositional flux can be derived from the ^{10}Be flux exported by rivers (Brown et al., 1988). However, a major obstacle arises from the grain size dependence of ^{10}Be concentrations in river sediment as Be adsorption depends on particle surface area (Singleton et al., 2016; Wittmann et al., 2012), more specifically, on adsorption site density (Maher and von Blanckenburg, 2016). As such, we adopted the isotopic ratio of ^{10}Be to ^{9}Be which is independent of mineralogical sorting, sorption capacity, and Be retentivity (Wittmann et al., 2012). We rearranged the equation for calculating denudation rates using ^{10}Be (meteoric)/^{9}Be ratios (von Blanckenburg et al., 2012) to solve for F_{met}:

$$F_{met} = D \times \left(\frac{^{10}Be}{^{9}Be}\right)_{reac} \times [\,^{9}Be]_{parent} \times f^{9}_{reac+diss} \times (1-e^{-\lambda t_s}) \quad (3)$$

where D (kg/m^2/yr) is the independently known catchment-wide denudation rate, (^{10}Be/^{9}Be)$_{reac}$ is the concentration ratio of ^{10}Be (at/kg) to ^{9}Be (mg/kg) measured in the reactive fraction of river sediments

(adsorbed onto or precipitated in secondary minerals). $[^{9}Be]_{parent}$ (mg/kg) comprises the ^{9}Be present in the parent bedrock prior to weathering, determined by assuming a value of the average upper continental crust (2.5 ± 0.5 mg/kg) (von Blanckenburg et al., 2012) or by measuring local bedrock samples in small catchments (Dannhaus et al., 2018; Deng et al., 2020). $f^{9}_{reac+diss}$ represents the mobile flux fraction of ^{9}Be that is released from primary minerals during weathering and measured in the sediment reactive fraction and dissolved fraction. Radioactive decay of ^{10}Be is negligible if the timescale of sediment transfer and storage (t_s) is short compared to its half-life.

We compiled literature meteoric ^{10}Be and ^{9}Be data of river sediment with *in situ* cosmogenic ^{10}Be data nearby, which was used as an independent estimate of D in Eq. (3). This dataset covers a wide spatial range (Fig. 1), including the Amazon River basin in South America (Wittmann et al., 2015), the Potomac River basin in USA (Portenga et al., 2019), the Zhuoshui River in Taiwan Island (Deng et al., 2020), the Ganga River basin in South Asia (Rahaman et al., 2017), and small catchments in the Slavkov Forest of Czech Republic (Dannhaus et al., 2018). The reported water pH was >7, suggesting a low dissolved Be flux, in most of studied rivers except for catchments in the Czech Republic, where the dissolved Be loss was corrected to calculate $f^{9}_{reac+diss}$ (Dannhaus et al., 2018). All these ^{10}Be measurements were based on the standard KNSTD07 or equivalents, and the used rock density was normalized to 2.65 g/cm^3.

2.5 Discrimination of ^{10}Be delivery effects

We discriminate between additive and dilution effects using a simple mass balance framework of water vapor and ^{10}Be in the "source" (condensation) and the "sink" (precipitation). Details of mass balance equations are provided in Appendix 1. In general, the ^{10}Be concentration of wet deposition is described by the ratio of the ^{10}Be production flux from the upper atmosphere (F_{prod}, in at/m^2/yr) to the condensation rate in the vapor source area (C, in m^3/m^2/yr) (Fig. 3). The difference in F_{met} between additive and dilution effects lies in the travel distance of moist air mass, illustrated by the ratio of surface area of condensation (A_c, in m^2) to area exposed to precipitation (A_p, in m^2). A_c/A_p ratios close to unity and >>1 indicate dominance of dilution effect and additive effect, respectively.

In a diagram of $[^{10}Be]_{wet}$ versus 1/P, a dilution effect is illustrated by an A_c/A_p of 1 and co-variation of P with C, resulting in a slope (at/m^2/yr) equal to the ^{10}Be production flux F_{prod}, i.e. a constant F_{met} (Fig. 3a) (Willenbring and von Blanckenburg, 2010b). In contrast, a pure additive effect results in a zero-slope relationship in that diagram where differences in P result from differences in A_c/A_p, and the y-intercept (at/m^3) is equal to F_{prod}/C, resulting in a constant $[^{10}Be]_{wet}$ for a given C (Fig. 3c).

In practice, the variable behaviors of moist air masses carrying both vapor and ^{10}Be will lead to a combination of delivery effects. When both A_c/A_p and C vary over the observation timescale, a mixture of dilution and additive effects may result. In this case, the ^{10}Be flux can be separated into two components: one component with unity A_c/A_p ratio (stable vapor source) and constant ^{10}Be flux (dilution component), and the other with constant condensation rate and thus constant $[^{10}Be]_{wet}$ (additive component). In the $[^{10}Be]_{wet}$ versus 1/P diagram the dilution component is identified from the slope (Fig. 3) and the additive component from the y-intercept. For a mixture of dilution and additive components, the proportion of the additive component (f_{add}, %) relative to the total ^{10}Be flux can be calculated as:

$$f_{add} = (\text{intercept} \times P)/(\text{intercept} \times P + \text{slope}) \times 100\% \quad (4)$$

This relationship shows that when P gets very high and there is a y-intercept resulting from the additive effect, intercept × P >> slope and f_{add} will be close to 100%. The framework developed also allows taking dry and dust ^{10}Be components into consideration. In their presence the slope in the $[^{10}Be]_{wet}$-1/P diagram (Figs. 3a-c) will steepen, because dry-dust ^{10}Be depositional fluxes are independent of precipitation rate and contribute as a component diluted by precipitation. Although mixing between additive and dilution effects can be shown by modern precipitation records (Eq. (4)), this mixing process also presents in millennial-scale records and may vary with time.

3. Results: latitudinal distribution of ^{10}Be depositional fluxes

All fluxes compiled from different approaches are shown as normalized to a common Holocene production rate in Fig. 4, and both the original and the re-normalized ^{10}Be fluxes are provided in Supplementary dataset.

From the GCM output, the Holocene depositional fluxes, averaged over a given latitude band, are within a relatively narrow range for latitudes from 0° to 50°, ranging from 0.88×10^6 to 1.55×10^6 at/cm^2/yr. The peak of GCM-derived flux is located at ~40° and can be explained by a higher air mass contribution from the stratosphere, which is the major reservoir (~65% of the total) of meteoric ^{10}Be (Heikkilä et al., 2013a).

From precipitation collections we recalculated ^{10}Be depositional fluxes based on Eq. (1). Contemporary ^{10}Be depositional fluxes from reliable records (filled symbols) generally increase from low to high latitudes, with a range of 0.42 to 5.30×10^6 at/cm^2/yr between latitudes of 10.4° and 47.3°. The reported percentage of recycled ^{10}Be from eolian dust, calculated by different methods for the dataset in New Zealand (35-50°N), Switzerland (46-47°N) and USA (30-50°N), varies from 6.2% to 35% (see Table S1 in Supplementary materials). Given the differences in dust correction methods employed and the substantial uncertainties resulting thereof, total ^{10}Be depositional fluxes are reported instead of fluxes corrected for recycled fractions. As such, these estimates can be directly compared to fluxes from soil profiles and riverine export where the recycled fraction is also included.

We also recalculated the ^{10}Be flux for comparison based on an empirical equation for estimating primary ^{10}Be fallout derived from data fitting between precipitation rate and precipitation ^{10}Be fluxes at mid-low latitudes (Graly et al., 2011):

$$F_{met}=P\times(1.44/(1+EXP((30.7-L)/4.36))+0.63)\times10^{10} \quad (5)$$

where L is latitude (°) and P is precipitation rate (m^3/m^2/yr). The recycled ^{10}Be component (dust contribution) was subtracted here. The derived fluxes, originally rescaled to global production rate based on a ϕ of 700 MeV (Graly et al., 2011), were re-normalized to an average Holocene rate following

normalization steps 2) and 3) in Section 2.2 for comparison with other approaches. The latitudinal trend of precipitation collections is mirrored by this fitting equation (Graly et al., 2011) as expected (correlation: $R = 0.60$, $p < 0.001$) given that this fitting equation is derived from the same dataset.

Based on Eq. (2), we recalculated ^{10}Be depositional fluxes from soil profiles. These millennial-scale fluxes from reliable records (filled symbols) vary from 0.12×10^6 to 4.07×10^6 at/cm^2/yr. No clear trend with latitude is apparent from soil-derived fluxes as observations exist in only few latitudinal bands. Low soil pH (<4) may lead to non-negligible loss of dissolved ^{10}Be (Maher and von Blanckenburg, 2016) and thus may bias the soil-derived ^{10}Be flux to lower values. According to those studies providing soil pH data, pH of representative soil profiles were between 6 and 8 in Hawaii (~20^{o}N) (Dixon et al., 2018), above 5 in the USA (40-45^{o}N) (Ouimet et al., 2015), and between 3 and 5 in the European Alps (45-50^{o}N) (Egli et al., 2010). Hence, some soil-derived ^{10}Be fluxes in the European Alps might only provide a lower limit. In general, for a given latitudinal band the precipitation-derived fluxes are higher than the soil-derived estimates.

Based on Eq. (3), ^{10}Be fluxes over a larger spatial scale, that is the river basin-scale, are evaluated. Riverine ^{10}Be fluxes derived from ^{10}Be (meteoric)/^{9}Be ratios increase with latitude (1° to 30°) and range from 0.24 to 5.74×10^6 at/cm^2/yr, and become quite scattered at 38-40° (the Potomac Basin) with a mean value of 1.84×10^6 at/cm^2/yr. At a higher latitude of ~50° (Czech Republic), riverine ^{10}Be fluxes decrease to 0.44-1.18×10^6 at/cm^2/yr. Riverine fluxes from the single isotopic system (meteoric ^{10}Be) are also provided in Supplementary dataset, but are not discussed below.

4. Discussion

4.1. Precipitation collections: dilution or additive effect?

Based on the published precipitation ^{10}Be dataset and the framework developed in Section 2.5, we can investigate the delivery effect on ^{10}Be depositional flux over monthly and annual scales. For New Zealand (2 years of observation) and Switzerland (7 years of observation), monthly-measured ^{10}Be data

303 are grouped based on sampling seasons and fitted separately (Fig. 5). The slopes are distinct between
304 seasons. The higher slopes in spring and summer are consistent with the seasonal cycles of stratosphere-
305 troposphere exchange, because more ^{10}Be-enriched stratospheric air is injected into the lower atmosphere
306 in spring and summer (Graham et al., 2003; Heikkilä et al., 2008a). Both in New Zealand and in
307 Switzerland the intercept and the slope show non-zero values, indicating a mixture of additive and
308 dilution components. To derive a representative f_{add} over a certain timescale (seasonal or annual scale), we
309 used the median precipitation rate of all measurements over this period for P in Eq. (4). For New Zealand
310 the resulting f_{add} shows a clear seasonal trend, with lower f_{add} in spring and summer (49-61%) than in
311 autumn and winter (74-87%). For Switzerland, the resulting f_{add} is also lower in spring and summer (59-
312 64%) than in autumn and winter (73-79%). The weaker additive effect in spring and summer can be
313 explained by more frequent occurrence of convective precipitation (dominated by the dilution effect)
314 during this period.

315 The dataset where ^{10}Be fluxes integrated from annual records are available can be used to detect the
316 delivery effect over a larger spatial range (Fig. 6). In mid-latitudes (30-50°) a mixture of additive and
317 dilution components exists in islandic (New Zealand) and continental (USA and Switzerland) settings,
318 and the f_{add} are 59% and 62%, respectively. Note that the dilution effect (the slope of the fit line in Fig. 6)
319 cannot be caused solely by dry and recycled ^{10}Be components. The range of published recycled ^{10}Be
320 fluxes estimated in the two settings is 0.11-0.33×10^6 at/cm^2/yr (Table S1 in Supplementary materials),
321 and the maximum ^{10}Be dry depositional flux derived from the preindustrial GCM model run is ~0.19×10^6
322 at/cm^2/yr (Heikkilä et al., 2013b). As such, the contribution of dry and recycled fluxes (0.30-0.52×10^6
323 at/cm^2/yr) is much lower than the slope of 0.94-1.00×10^6 at/cm^2/yr in the two settings (Fig. 6). In Kikai
324 Island at ~28° the relatively low slope and comparatively high intercept indicate the dominance of an
325 additive effect, perhaps caused by the high precipitation rate within the observation period. For the dataset
326 at 10-30° (mainly from India), the negative intercept can be explained with F_{prod} (Eq. (A3)) differing

between sampling stations, as this dataset shows a wide range in latitude and a positive correlation (R^2=0.60) between latitude and ^{10}Be depositional flux.

Overall, our re-analysis of precipitation ^{10}Be data shows that a mixture of additive and dilution components could be present in both continental and islandic settings. Additionally, the proportion of the additive component seems to decrease with a longer integration timescale. Based on the ECHAM5-HAM output, the ^{10}Be deposition variability is dominated by precipitation rate over the seasonal scale, but when averaging out the seasonal cycle on multiannual scale, the ^{10}Be deposition mainly reflects ^{10}Be production variability rather than precipitation rate (Heikkilä and Smith, 2013), suggesting a larger dilution component and lower f_{add}. Our analysis is broadly consistent with these modeling results, showing that annual-scale f_{add} (59% and 62%) in both New Zealand and Switzerland is at the lower limit of the seasonal f_{add} range (49-87% and 59-79%, respectively). The potential reason is that the A_c/A_p ratio over multiannual scale may be more stable due to averaging of seasonal variability in vapor sources. Nevertheless, longer time-series precipitation ^{10}Be records (e.g. decadal-scale) are needed to confirm this temporal variation in f_{add}. In any case, this analysis highlights that the dilution effect does not necessarily dominate global ^{10}Be precipitation records (Willenbring and von Blanckenburg, 2010b). Also, the empirical equation derived from data fitting between F_{met} and P (Graly et al., 2011) may not result in representative fluxes, because such treatment implicitly assumes a sole additive effect which is mostly not the case.

4.2. Comparing precipitation- with GCM- derived ^{10}Be fluxes

We next compare ^{10}Be fluxes determined from precipitation, soil, and river sediment with those derived from GCM modeling (Fig. 7). We do so not because we believe the GCM-derived dataset serves as a benchmark that all other estimates should match, but rather, because of its global spatial coverage making it the only dataset to allow comparison with all other datasets.

The precipitation-derived fluxes are plotted against GCM-derived fluxes as shown in Fig. 7a. In general, no clear correlation between precipitation- and GCM- derived fluxes is apparent, and the range in precipitation records (0.42-5.30×10^6 at/cm^2/yr) is much larger than that in GCM-derived fluxes (0.66-2.20×10^6 at/cm^2/yr). Almost half of precipitation records are >2 times greater than the corresponding GCM-derived fluxes; 43% of precipitation-derived data are 1-2 times of GCM-derived fluxes, and only 8% of precipitation-derived data is lower than the GCM-derived fluxes (Fig. 7a). This general pattern of significantly higher precipitation-derived fluxes ($p < 0.001$ from a two-sided Wilcoxon signed-rank test) is independent of location (Fig. 7a). The large variability of precipitation-derived fluxes is consistent with their sensitivity to short-term (10^0-10^1 yr) local variations in atmospheric dynamics, such as vapor sources and stratosphere-troposphere exchange. Hence, observations of only 1-2 years may not capture the millennial-scale ^{10}Be depositional signal required for geomorphic applications.

4.3. Comparing soil- with GCM- derived ^{10}Be fluxes

Over millennial timescale, the relation between soil-derived and GCM-derived fluxes for each latitudinal zone is shown in Fig. 7b. Most of flux data in the "excluded" series yield lower values than other soil data or corresponding GCM-derived fluxes. The potential deficits in ^{10}Be fluxes can be explained by incomplete sampling of the depth profile or ^{10}Be loss through surface erosion. For each reliable data series, no correlation between fluxes derived from both methods can be observed, and the range of soil-derived fluxes (0.11-4.07×10^6 at/cm^2/yr) is larger than that of GCM-derived fluxes (1.08-2.55×10^6 at/cm^2/yr). Specifically, GCM-derived data averages over a large grid size (~10^2 km) and may not fully capture the distinct local variability of ^{10}Be delivery in Hawaii where precipitation rates increase by one order of magnitude within a short distance (~20 km) (Dixon et al., 2018). The ratio of soil-derived flux to GCM-derived flux is generally lower than 1 ($p < 0.05$) and varies within a narrow range between 0.48 and 0.90 for average value of each data series. Also, it is worth noting that more than half (57%) of the soil-derived fluxes agree with GCM-derived fluxes within a factor of 2.

4.4. Comparing riverine with GCM-derived ^{10}Be fluxes

Over the river basin scale, riverine export fluxes derived from ^{10}Be (meteoric)/^{9}Be ratios are compared with GCM-derived meteoric ^{10}Be fluxes (Fig. 7c). The riverine output of meteoric ^{10}Be agrees with atmospheric input within a factor of ~2 for each data series, ranging from 0.52 (on average) in the Amazon basin to 1.78 (on average) in the Ganga basin (Fig. 7c). Reasons for a weaker agreement for some samples comprise, for example: 1) coarse-grained quartz used for *in situ* ^{10}Be measurement (to determine D in Eq. (3)) may be derived from a different sediment source compared to fine-grained sediment used for ^{10}Be (meteoric)/^{9}Be measurement, or multiple grain size fractions analyzed for ^{10}Be (meteoric)/^{9}Be differ in source even at the same location (Wittmann et al., 2015); 2) In basins where no $[^{9}Be]_{parent}$ was measured directly and the drainage area is not large enough to average out lithological heterogeneity (e.g. small sub-basins of <100 km^2 in the Potomac River, USA), the resulting riverine fluxes could be biased by variations in $[^{9}Be]_{parent}$. Nevertheless, although the riverine ^{10}Be fluxes are generally lower than GCM-derived values ($p < 0.001$), the majority (71%) of the two estimates indeed fall within a close range (between 2:1 and 1:2 lines) (Fig. 7c).

4.5. Evaluation of ^{10}Be depositional fluxes from multiple approaches

To provide a more in-depth comparison between different approaches, we selected three regions where both precipitation- and soil- derived ^{10}Be depositional fluxes exist within a narrow latitudinal band such that both can be compared between each other and with GCM-derived fluxes (Fig. 8). The riverine data is not included as its spatial scale by far exceeds the more local scale over which precipitation or soil ^{10}Be data integrate. The selected regions include New Zealand (36-46°S), the interior USA (40-45°N) and the European Alps (46-47°N), covering continental and islandic settings. All flux data were normalized to an average Holocene ^{10}Be production rate.

Over the annual scale, precipitation-derived ^{10}Be fluxes from the three regions are in close agreement and provide a mean flux of 3.01×10^{6} at/cm^2/yr. The relative standard deviation of ^{10}Be fluxes varies from 14-17% (New Zealand and European Alps) to 31% (interior USA). Over the millennial scale, the soil-derived ^{10}Be fluxes are generally lower than the precipitation-derived ^{10}Be fluxes (Fig. 8), and amount to

400 1.28×10^6 at/cm^2/yr on average. On a similar (Holocene) timescale, GCM-derived ^{10}Be fluxes, with a
401 mean value of 1.76×10^6 at/cm^2/yr in the three regions, fall between precipitation- and soil- derived fluxes.
402 Overall, the ratio of average precipitation-derived flux to average GCM-derived flux varies from 1.4 to
403 1.9. The ratio of average soil-derived flux to average GCM-derived flux falls within a range of 0.5-1.1.

404 Bearing in mind that all data were normalized to ^{10}Be production rates with identical solar
405 modulation and magnetic field strength, the fact that ^{10}Be depositional fluxes from precipitation
406 collections are highest might be caused by a short-term, transient enhancement of ^{10}Be delivery that is
407 averaged-out over longer timescales (e.g. millennia). Such enhancement may potentially be caused by a
408 transient increase in atmospheric aerosol loading (e.g. from Be scavenging) today due to anthropogenic
409 emission (Dentener et al., 2006). However, this scenario contradicts the findings from GCM modeling,
410 where the difference in GCM-derived fluxes between industrial and early Holocene runs at each site are
411 relatively small (e.g. <~40%), despite of much higher (~5 fold) aerosol loading used in the industrial run
412 (Heikkilä and Smith, 2013). The reason for the low forcing of aerosol loading on ^{10}Be delivery is that the
413 atmospheric sulfate burden exceeds that of ^{10}Be by several orders of magnitude under both industrial and
414 pre-industrial conditions (Field et al., 2006; Heikkilä et al., 2013a), and hence ^{10}Be delivery is production-
415 rather than sulfate-scavenging limited. We can therefore discount this explanation.

416 Another possibility is that the modern enhancement of ^{10}Be delivery is a bias introduced through a
417 dependence of precipitation on observational interval. In fact, it was suggested that the precipitation rate
418 depends on measurement interval due to hiatuses (i.e. periods without precipitation) following a power
419 law distribution (Wilkinson, 2015). Over a measurement interval of several years or less, precipitation
420 rate and measurement interval scale by a negative power law, that is, higher precipitation rates are
421 apparent over shorter measurement intervals. This power law behavior emerges from the stochastic nature
422 of synoptic weather systems (Wilkinson, 2015). In contrast, over longer timescales (e.g. decades or
423 longer), the precipitation rate gradually settles to a constant value that reflects the long-term regional
424 climate, and is independent of measurement interval (Wilkinson, 2015). In other words, this measurement

interval bias is not present over a larger spatial or longer temporal span (Sadler and Jerolmack, 2015), such as in GCM and soil profiles, where precipitation rates are deterministic rather than stochastic.

We explore how such measurement interval bias on precipitation rates affects ^{10}Be delivery. This bias will only affect the additive component of the ^{10}Be flux because the dilution component does not depend on precipitation rate. Because of the higher precipitation rate over shorter intervals (10^0-10^1 yr) (Wilkinson, 2015), and if this results from long-distance transport of vapor, the additive ^{10}Be component f_{add} (Eq. (4)) will increase accordingly and a higher delivery flux of ^{10}Be will result. Conversely, the measurement interval bias also offers a hypothesis for the lower soil-derived ^{10}Be fluxes compared to precipitation-derived fluxes: the additive component is suggested to decrease with increasing integration time-interval (Section 4.1) and thus should account for a lower proportion in soil-derived ^{10}Be fluxes integrating over 10^4-10^5 yrs. When corrected for temporal changes of ^{10}Be production, the dilution component of the ^{10}Be flux is expected to be time-invariant, and will correspond to the dilution flux contained in precipitation collections. In practice, we can use this assumption to estimate f_{add} over the timescale integrated by soil profiles. The additive component of the ^{10}Be depositional flux determined on soils is calculated as the difference between total soil-derived flux and the dilution component of precipitation-derived flux (i.e. slope values in Fig. 6). The resulting proportions of the additive component (f_{add}) for soil profiles in New Zealand (42%) and USA (31%) are indeed much lower than those derived from precipitation records in Fig. 6 (59-62%). In the European Alps the total soil-derived flux (0.76×10^6 at/cm^2/yr) is even lower than the precipitation-derived dilution component (1.00×10^6 at/cm^2/yr, Fig. 6). This deficit might hint at a very small additive effect combined with potential loss of soil ^{10}Be inventory because of the low soil pH (3-5).

The conclusion of these considerations is that, as most geomorphologic processes integrate over millennial scale, ^{10}Be fluxes from soil profiles rather than precipitation collections provide the most relevant estimate, given their potential to record a representative additive effect over millennia.

Finally, we explore why GCM-derived fluxes commonly exceed soil-derived fluxes (Fig. 8). One explanation is that soil-derived ^{10}Be depositional flux provides an underestimate, because the assumption of full ^{10}Be retention may be invalid (Graly et al., 2011; Maher and von Blanckenburg, 2016). Another explanation is that GCMs provide overestimated fluxes because the production function (Masarik and Beer, 2009) adopted by the GCM (Heikkilä and Smith, 2013) may overestimate (e.g. ~15% higher under a ϕ of 550 MeV) the global production rate of ^{14}C (Kovaltsov et al., 2012), and presumably also ^{10}Be. Since the design of these models, production rates of cosmogenic nuclides by heavier nuclei (atom number $\geq$ 2) have been revised downwards (Kovaltsov et al., 2012). To conclude, we suggest that the "true" ^{10}Be depositional flux representative for the millennial scale lies between soil-derived and GCM-derived fluxes reported here.

5. Conclusions

Our re-analysis of ^{10}Be flux estimates from four independent methods provides important conceptual insights for the use of meteoric ^{10}Be in Earth surface studies. These are:

1) Contemporary ^{10}Be flux records (precipitation collections) are subject to both a dilution effect and an additive effect. The weight of either effect depends on the area ratio of vapor condensation to precipitation and the prevailing condensation rate. Based on existing precipitation records integrating over the seasonal scale, we estimate the proportion of the additive component to be higher in autumn and winter (up to 87%); over the annual scale, an additive component of ~60% is found in islandic and continental settings. Because only the additive effect depends on precipitation rate, the empirical fitting between ^{10}Be fluxes and precipitation rates assuming a sole additive effect likely overestimates the control of precipitation on ^{10}Be delivery.

2) ^{10}Be flux estimates that average over 10^3 to 10^5 years, like those from soil profiles and river fluxes, agree with GCM-derived fluxes within a factor of 2, but can be less than half of the modern ^{10}Be fluxes from precipitation collections. A possible negative power-law relationship between precipitation rates and

measurement interval over short timescales (10^0-10^1 yr), combined with a ^{10}Be additive effect, can explain higher ^{10}Be fluxes in short-term precipitation collections. Over a longer timescale (10^4-10^5 yrs) the additive component can decrease to 30-40%. Because most geomorphologic processes integrate over millennial timescales, ^{10}Be fluxes from soil profiles, in contrast to precipitation collections, likely provide the most relevant estimate, given their representative estimation of the additive effect over millennia.

3) GCM-derived ^{10}Be fluxes commonly exceed soil-derived fluxes. The soil-derived fluxes might represent an underestimate due to potential partial retention of ^{10}Be. GCM on the other hand might overestimate the flux by using outdated spectra of the heavier nuclei component of cosmic rays. We conclude that the best estimate for the millennial-scale ^{10}Be depositional flux lies between soil- and GCM- derived fluxes.

For producing new ^{10}Be flux data, we recommend that more efforts should be spent on soil profiles as published data are still rare, and many of these do not meet the stringent requirements for flux calculation. The chosen soil profiles should meet the following criteria: minimum surface erosion, high soil pH, low ^{10}Be inheritance, and sufficient sampling depth for quantification of the inheritance. If these conditions can be met, ^{10}Be flux estimates from soil profiles are the method of choice.

Acknowledgements

We thank Joseph Graly and two anonymous reviewers for their valuable comments and Louis Derry for the editorial handling of the manuscript. KD thanks the support by the National Natural Science Foundation of China (Grant 41991324) and also the Freie Universität Berlin-China Scholarship Council (FUB-CSC) PhD Program for his scholarship in Germany.

Appendix 1 A mass balance framework for ^{10}Be delivery effects

The total ^{10}Be deposition is comprised of wet deposition of $^{10}Be(OH)_2$ scavenged by precipitation, dry deposition of $^{10}Be(OH)_2$ by friction-based aerosol deposition, and recycled ^{10}Be attached to dust. When neglecting dry and recycled components, we can balance water vapor and ^{10}Be between vapor

497 "source" (condensation) and "sink" (precipitation). We conceptually describe the vapor accumulation to
498 be the product of the water condensation rate C ($m^3/m^2/yr$) and the surface area of condensation A_c (m^2),
499 which is balanced by precipitation as calculated by the product of the precipitation rate P ($m^3/m^2/yr$) and
500 the area exposed to precipitation A_p (m^2):

501 $$C \times A_c = P \times A_p \quad \text{(A1)}$$

502 and thus the precipitation rate P is

503 $$P = C \times (A_c/A_p) \quad \text{(A2)}$$

504 The ^{10}Be production flux from the upper atmosphere is F_{prod} ($at/m^2/yr$), and the total flux of ^{10}Be
505 accumulating in a given moist air mass is proportional to the area A_c where vapor also condenses. The
506 ^{10}Be concentration of wet deposition ($[^{10}Be]_{wet}$, in at/m^3) in the condensation area is

507 $$[^{10}Be]_{wet} = (F_{prod} \times A_c)/(C \times A_c) = F_{prod}/C \quad \text{(A3)}$$

508 In the dilution effect, both vapor condensation and ^{10}Be accumulation take place over the same area
509 as precipitation due to rapid water turnover (e.g. convective precipitation), and thus $A_c = A_p$. Hence, the
510 meteoric delivery flux is:

511 $$F_{met} = [^{10}Be]_{wet} \times P = F_{prod} \quad \text{(A4)}$$

512 In the additive effect, in contrast, moist air mass accumulating both vapor and ^{10}Be is advected over
513 extended distances (e.g. cyclonic precipitation), and $A_c > A_p$. The meteoric delivery flux is:

514 $$F_{met} = [^{10}Be]_{wet} \times P = F_{prod} \times (A_c/A_p) \quad \text{(A5)}$$

515 Thus, the difference in F_{met} between additive and dilution effects is whether the A_c/A_p ratio (related
516 to the travel distance of moist air mass) controls the precipitation rate (Eq. (A2)) and ^{10}Be accumulation in
517 moist air mass. Eqs. (A4-A5) form the base for a practical evaluation of the ^{10}Be delivery effect from
518 combined measurements of ^{10}Be concentration in precipitation and the precipitation rate.

519

520 **References:**

521 Bacon, A.R., Richter, D.d., Bierman, P.R., Rood, D.H., 2012. Coupling meteoric 10Be with pedogenic
522 losses of 9Be to improve soil residence time estimates on an ancient North American interfluve.
523 Geology 40, 847-850.

524 Balco, G.A., 2004. The sedimentary record of subglacial erosion beneath the Laurentide Ice Sheet.
525 University of Washington.

526 Brown, E.T., Edmond, J.M., Raisbeck, G.M., Bourlès, D.L., Yiou, F., Measures, C.I., 1992. Beryllium
527 isotope geochemistry in tropical river basins. Geochim. Cosmochim. Acta 56, 1607-1624.

528 Brown, L., Pavich, M.J., Hickman, R., Klein, J., Middleton, R., 1988. Erosion of the eastern United States
529 observed with 10Be. Earth Surf. Processes Landforms 13, 441-457.

530 Chmeleff, J., von Blanckenburg, F., Kossert, K., Jakob, D., 2010. Determination of the 10 Be half-life by
531 multicollector ICP-MS and liquid scintillation counting. Nucl. Instrum. Methods Phys. Res., Sect. B
532 268, 192-199.

533 Christl, M., Lippold, J., Steinhilber, F., Bernsdorff, F., Mangini, A., 2010. Reconstruction of global 10 Be
534 production over the past 250 ka from highly accumulating Atlantic drift sediments. Quat. Sci. Rev.
535 29, 2663-2672.

536 Dannhaus, N., Wittmann, H., Krám, P., Christl, M., Von Blanckenburg, F., 2018. Catchment-wide
537 weathering and erosion rates of mafic, ultramafic, and granitic rock from cosmogenic meteoric
538 10Be/9Be ratios. Geochim. Cosmochim. Acta 222, 618-641.

539 Deng, K., Yang, S., von Blanckenburg, F., Wittmann, H., 2020. Denudation Rate Changes Along a Fast-
540 Eroding Mountainous River With Slate Headwaters in Taiwan From 10Be (Meteoric)/9Be Ratios.
541 Journal of Geophysical Research: Earth Surface 125, e2019JF005251.

542 Dentener, F., Kinne, S., Bond, T., Boucher, O., Cofala, J., Generoso, S., Ginoux, P., Gong, S.,
543 Hoelzemann, J.J., Ito, A., Marelli, L., Penner, J.E., Putaud, J.P., Textor, C., Schulz, M., van der Werf,

G.R., Wilson, J., 2006. Emissions of primary aerosol and precursor gases in the years 2000 and 1750 prescribed data-sets for AeroCom. Atmos. Chem. Phys. 6, 4321-4344.

Dixon, J.L., Chadwick, O.A., Pavich, M.J., 2018. Climatically controlled delivery and retention of meteoric 10Be in soils. Geology 46, 899-902.

Egli, M., Brandová, D., Böhlert, R., Favilli, F., Kubik, P.W., 2010. 10Be inventories in Alpine soils and their potential for dating land surfaces. Geomorphology 119, 62-73.

Field, C.V., Schmidt, G.A., Koch, D., Salyk, C., 2006. Modeling production and climate-related impacts on Be-10 concentration in ice cores. Journal of Geophysical Research-Atmospheres 111, 1-13.

Graham, I., Ditchburn, R., Barry, B., 2003. Atmospheric deposition of 7Be and 10Be in New Zealand rain (1996-98). Geochim. Cosmochim. Acta 67, 361-373.

Graly, J.A., Reusser, L.J., Bierman, P.R., 2011. Short and long-term delivery rates of meteoric 10Be to terrestrial soils. Earth Planet. Sci. Lett. 302, 329-336.

Heikkilä, U., Beer, J., Abreu, J.A., Steinhilber, F., 2013a. On the Atmospheric Transport and Deposition of the Cosmogenic Radionuclides (10 Be): A Review. Space Sci. Rev. 176, 321-332.

Heikkilä, U., Beer, J., Alfimov, V., 2008a. Beryllium-10 and beryllium-7 in precipitation in Dübendorf (440 m) and at Jungfraujoch (3580 m), Switzerland (1998-2005). Journal of Geophysical Research Atmospheres 113, 1-10.

Heikkilä, U., Beer, J., Feichter, J., 2008b. Meridional transport and deposition of atmospheric 10Be. Atmospheric Chemistry & Physics 8, 16819-16849.

Heikkilä, U., Phipps, S.J., Smith, A.M., 2013b. Be-10 in late deglacial climate simulated by ECHAM5-HAM - Part 1:;Climatological influences on Be-10 deposition. Clim. Past 9, 2641-2649.

Heikkilä, U., Smith, A.M., 2013. Production rate and climate influences on the variability of 10Be deposition simulated by ECHAM5-HAM: Globally, in Greenland, and in Antarctica. Journal of Geophysical Research: Atmospheres 118, 2506-2520.

568 Heikkilä, U., von Blanckenburg, F., 2015. The global distribution of Holocene meteoric 10Be fluxes from
569 atmospheric models. Distribution maps for terrestrial Earths surface applications, GFZ Data Services,
570 GFZ Potsdam, Germany.
571 Jungers, M.C., Bierman, P.R., Matmon, A., Nichols, K., Larsen, J., Finkel, R., 2009. Tracing hillslope
572 sediment production and transport with in situ and meteoric 10Be. Journal of Geophysical Research:
573 Earth Surface 114.
574 Kovaltsov, G.A., Mishev, A., Usoskin, I.G., 2012. A new model of cosmogenic production of
575 radiocarbon 14C in the atmosphere. Earth Planet. Sci. Lett. 337-338, 114-120.
576 Lebatard, A.-E., Bourles, D.L., Braucher, R., Arnold, M., Duringer, P., Jolivet, M., Moussa, A.,
577 Deschamps, P., Roquin, C., Carcaillet, J., Schuster, M., Lihoreau, F., Likius, A., Mackaye, H.T.,
578 Vignaud, P., Brunet, M., 2010. Application of the authigenic Be-10/Be-9 dating method to
579 continental sediments: Reconstruction of the Mio-Pleistocene sedimentary sequence in the early
580 hominid fossiliferous areas of the northern Chad Basin. Earth Planet. Sci. Lett. 297, 57-70.
581 Maejima, Y., Matsuzaki, H., Higashi, T., 2005. Application of cosmogenic 10Be to dating soils on the
582 raised coral reef terraces of Kikai Island, southwest Japan. Geoderma 126, 389-399.
583 Maher, K., von Blanckenburg, F., 2016. Surface ages and weathering rates from 10Be (meteoric) and
584 10Be/9Be: Insights from differential mass balance and reactive transport modeling. Chem. Geol. 446,
585 70-86.
586 Mahowald, N.M., Baker, A.R., Bergametti, G., Brooks, N., Duce, R.A., Jickells, T.D., Kubilay, N.,
587 Prospero, J.M., Tegen, I., 2005. Atmospheric global dust cycle and iron inputs to the ocean. Global
588 Biogeochem. Cycles 19.
589 Mann, M., Beer, J., Steinhilber, F., Abreu, J.A., Christl, M., Kubik, P., 2011. Variations in the
590 depositional fluxes of cosmogenic beryllium on short time scales. Atmos. Environ. 45, 2836-2841.
591 Masarik, J., Beer, J., 2009. An updated simulation of particle fluxes and cosmogenic nuclide production
592 in the Earth's atmosphere. Journal of Geophysical Research: Atmospheres 114, 1-9.

593 Mckean, J.A., Dietrich, W.E., Finkel, R.C., Southon, J.R., Caffee, M.W., 1993. Quantification of soil
594 production and downslope creep rates from cosmogenic 10Be accumulations on a hillslope profile.
595 Geology 21, 343-346.
596 Monaghan, M.C., Krishnaswami, S., Turekian, K.K., 1986. The global-average production rate of 10 Be.
597 Earth Planet. Sci. Lett. 76, 279-287.
598 Nishiizumi, K., Imamura, M., Caffee, M.W., Southon, J.R., Finkel, R.C., McAninch, J., 2007. Absolute
599 calibration of 10Be AMS standards. Nucl. Instrum. Methods Phys. Res., Sect. B 258, 403-413.
600 Ouimet, W., Dethier, D., Bierman, P., Wyshnytzky, C., Shea, N., Rood, D.H., 2015. Spatial and temporal
601 variations in meteoric 10Be inventories and long-term deposition rates, Colorado Front Range. Quat.
602 Sci. Rev. 109, 1-12.
603 Pavich, M.J., Brown, L., Harden, J., Klein, J., Middleton, R., 1986. 10Be distribution in soils from
604 Merced River terraces, California. Geochim. Cosmochim. Acta 50, 1727-1735.
605 Portenga, E.W., Bierman, P.R., Trodick, C.D., Jr., Greene, S.E., DeJong, B.D., Rood, D.H., Pavich, M.J.,
606 2019. Erosion rates and sediment flux within the Potomac River basin quantified over millennial
607 timescales using beryllium isotopes. GSA Bulletin 131, 1295-1311.
608 Rahaman, W., Wittmann, H., von Blanckenburg, F., 2017. Denudation rates and the degree of chemical
609 weathering in the Ganga River basin from ratios of meteoric cosmogenic 10Be to stable 9Be. Earth
610 Planet. Sci. Lett. 469, 156-169.
611 Reusser, L., Graly, J., Bierman, P., Rood, D., 2010. Calibrating a long-term meteoric 10Be accumulation
612 rate in soil. Geophys. Res. Lett. 37.
613 Sadler, P.M., Jerolmack, D.J., 2015. Scaling laws for aggradation, denudation and progradation rates: the
614 case for time-scale invariance at sediment sources and sinks, in: Smith, D.G., Bailey, R.J., Burgess,
615 P.M., Fraser, A.J. (Eds.), Strata and Time: Probing the Gaps in Our Understanding, pp. 69-88.
616 Schmidt, G.A., Ruedy, R., Hansen, J.E., Aleinov, I., Bell, N., Bauer, M., Bauer, S., Cairns, B., Canuto, V.,
617 Cheng, Y., Del Genio, A., Faluvegi, G., Friend, A.D., Hall, T.M., Hu, Y., Kelley, M., Kiang, N.Y.,
618 Koch, D., Lacis, A.A., Lerner, J., Lo, K.K., Miller, R.L., Nazarenko, L., Oinas, V., Perlwitz, J.,

Perlwitz, J., Rind, D., Romanou, A., Russell, G.L., Sato, M., Shindell, D.T., Stone, P.H., Sun, S., Tausnev, N., Thresher, D., Yao, M.-S., 2006. Present-Day Atmospheric Simulations Using GISS ModelE: Comparison to In Situ, Satellite, and Reanalysis Data. Journal of Climate 19, 153-192.

Schoonejans, J., Vanacker, V., Opfergelt, S., Christl, M., 2017. Long-term soil erosion derived from in-situ 10Be and inventories of meteoric 10Be in deeply weathered soils in southern Brazil. Chem. Geol.

Singleton, A.A., Schmidt, A.H., Bierman, P.R., Rood, D.H., Neilson, T.B., Greene, E.S., Bower, J.A., Perdrial, N., 2016. Effects of grain size, mineralogy, and acid-extractable grain coatings on the distribution of the fallout radionuclides 7 Be, 10 Be, 137 Cs, and 210 Pb in river sediment. Geochim. Cosmochim. Acta 197, 71-86.

Somayajulu, B.L.K., Sharma, P., Beer, J., Bonani, G., Hofmann, H.J., Morenzoni, E., Nessi, M., Suter, M., Wölfli, W., 1984. 10Be annual fallout in rains in India. Nucl. Instrum. Methods Phys. Res., Sect. B 5, 398-403.

Steinhilber, F., Abreu, J.A., Beer, J., Brunner, I., Christl, M., Fischer, H., Heikkilä, U., Kubik, P.W., Mann, M., McCracken, K.G., Miller, H., Miyahara, H., Oerter, H., Wilhelms, F., 2012. 9,400 years of cosmic radiation and solar activity from ice cores and tree rings. Proceedings of the National Academy of Sciences 109, 5967-5971.

Stier, P., Feichter, J., Kinne, S., Kloster, S., Vignati, E., Wilson, J., Ganzeveld, L., Tegen, I., Werner, M., Balkanski, Y., 2005. The aerosol-climate model ECHAM5-HAM. Atmos. Chem. Phys. 5, 1125-1156.

von Blanckenburg, F., Bouchez, J., Ibarra, D.E., Maher, K., 2015. Stable runoff and weathering fluxes into the oceans over Quaternary climate cycles. Nat. Geosci. 8, 538-542.

von Blanckenburg, F., Bouchez, J., Wittmann, H., 2012. Earth surface erosion and weathering from the Be-10 (meteoric)/Be-9 ratio. Earth Planet. Sci. Lett. 351, 295-305.

Wilkinson, B.H., 2015. Precipitation as Meteoric Sediment and Scaling Laws of Bedrock Incision: Assessing the Sadler Effect. The Journal of Geology 123, 95-112.

644 Willenbring, J.K., von Blanckenburg, F., 2010a. Long-term stability of global erosion rates and
645 weathering during late-Cenozoic cooling. Nature 465, 211-214.
646 Willenbring, J.K., von Blanckenburg, F., 2010b. Meteoric cosmogenic Beryllium-10 adsorbed to river
647 sediment and soil: Applications for Earth-surface dynamics. Earth Sci. Rev. 98, 105-122.
648 Wittmann, H., von Blanckenburg, F., Bouchez, J., Dannhaus, N., Naumann, R., Christl, M., Gaillardet, J.,
649 2012. The dependence of meteoric Be-10 concentrations on particle size in Amazon River bed
650 sediment and the extraction of reactive Be-10/Be-9 ratios. Chem. Geol. 318, 126-138.
651 Wittmann, H., von Blanckenburg, F., Dannhaus, N., Bouchez, J., Gaillardet, J., Guyot, J.L., Maurice, L.,
652 Roig, H., Filizola, N., Christl, M., 2015. A test of the cosmogenic Be-10(meteoric)/Be-9 proxy for
653 simultaneously determining basin- wide erosion rates, denudation rates, and the degree of weathering
654 in the Amazon basin. J. Geophys. Res. 120, 2498-2528.

655

Figures

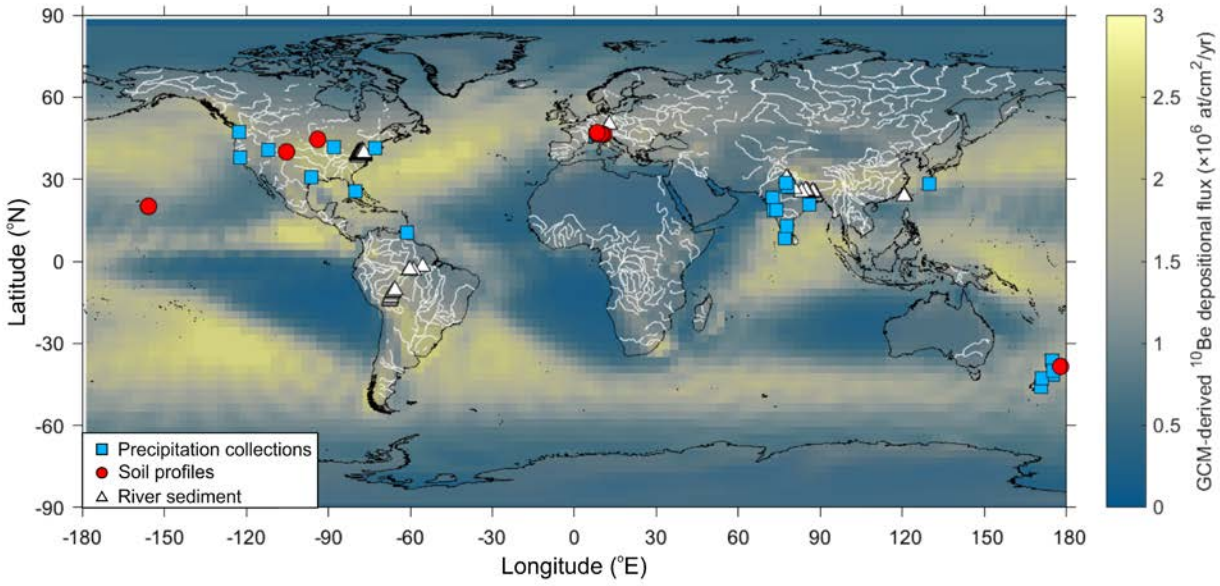

Fig. 1 The spatial distribution of flux data measured in precipitation collections (N=46), soil profiles (N=23) and river sediment (N=90). Data sources are described in detail in Section 2 and the flux data are provided in Supplementary dataset. The distribution map shows the GCM-derived ^{10}Be depositional flux from the ECHAM5-HAM model with the average ^{10}Be production and climatic conditions of the Holocene (Heikkilä and von Blanckenburg, 2015).

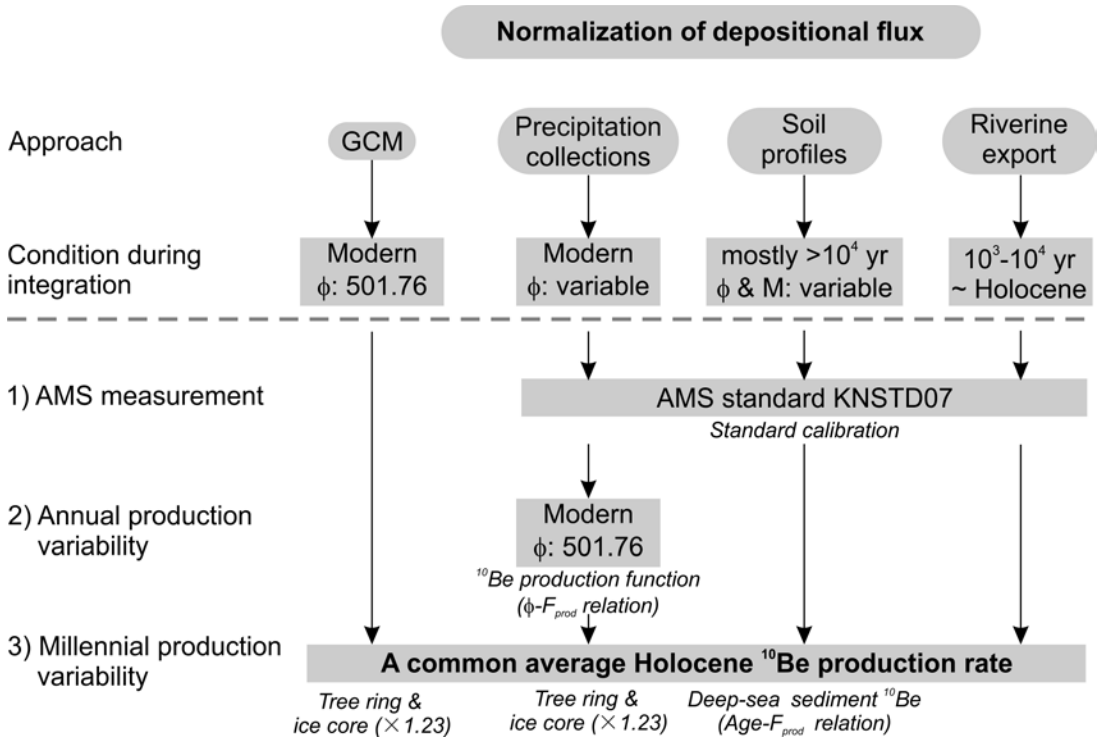

664

665 Fig. 2 Procedures for normalization of ^{10}Be depositional fluxes that account for analytical differences (1)
666 and temporal variations in the flux of galactic cosmic rays (2-3). The aim of these procedures is to
667 normalize all fluxes compiled from four approaches to a common Holocene ^{10}Be production rate from the
668 upper atmosphere (F_{prod}, in at/m^2/yr). ϕ is the solar modulation factor (MeV) and M the geomagnetic field
669 strength. 1) ^{10}Be concentrations are normalized to a common AMS standard (Nishiizumi et al. (2007). 2)
670 Given that ^{10}Be is well-mixed in the stratosphere after production (Heikkilä et al., 2013a; Heikkilä et al.,
671 2008b), we perform a global normalization using the modeled relationship between ϕ and global-averaged
672 production rate (Masarik and Beer, 2009). For precipitation collections, each annual depositional flux is
673 normalized using the average ϕ within the observation period to the modern ϕ of 501.76 MeV. 3)
674 Depending on the integration timescale of each approach, fluxes are normalized to an average Holocene
675 production rate using a variety of proxy records of ^{10}Be production that combine variations of both solar
676 modulation and magnetic field strength (See Fig. S1 in Supplementary materials). The ratio of average
677 Holocene production rate to the modern value at a ϕ of 501.76 MeV (~1.23) is derived from ^{10}Be
678 production proxy records from tree rings and ice cores (Steinhilber et al., 2012). The global ^{10}Be

679 production curve reconstructed from deep-sea sediments over longer term (since 250 ka) is sourced from
680 Christl et al. (2010). The riverine flux estimates were left un-normalized for F_{prod} variations as their
681 integration time scale is unknown and depends on denudation rate and infiltration depth of meteoric ^{10}Be
682 (Willenbring and von Blanckenburg, 2010b). It is considered to be typically 10^3-10^4 yrs, which is within
683 the Holocene reference timescale.

684

685

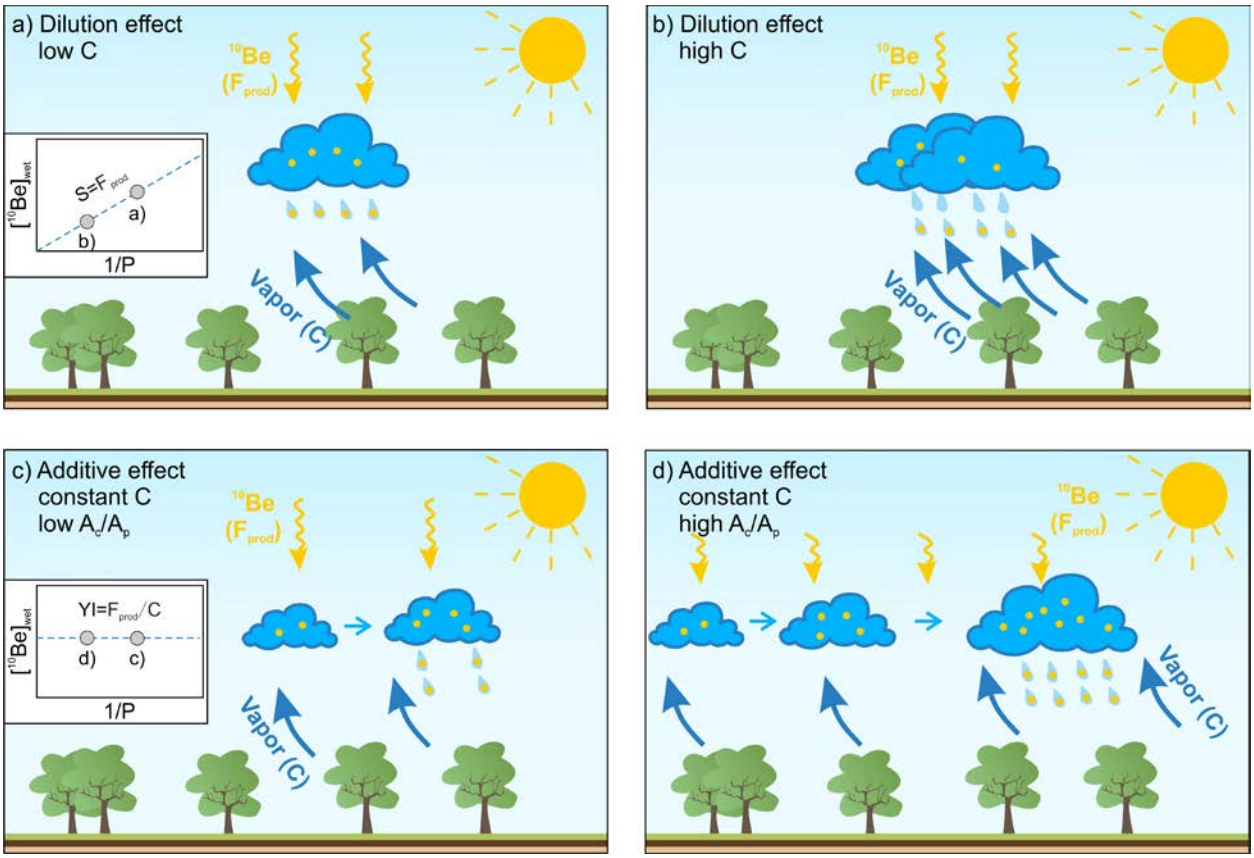

686

687 Fig. 3 Conceptual framework of ^{10}Be delivery. a) and b): the dilution effect is in operation when the ratio
688 of vapor source area (A_c) to area of precipitation event (A_p) is roughly unity, meaning that the vapor is of
689 local origin and also no ^{10}Be is advected from further distances. In that case the precipitation rate (P, blue
690 droplets) is equal to the condensation rate (C), and the ^{10}Be flux (yellow dots in droplets) is constant, but
691 the ^{10}Be concentration depends on the amount of dilution by vapor. The inset in a) shows the relation of
692 $[^{10}Be]_{wet}$ to 1/P for the dilution effect, and the slope (S, in at/m^2/yr) is equal to the atmospheric production
693 rate of ^{10}Be (F_{prod}). c) and d): the additive effect is in operation when the condensation rate C is constant,
694 but both the precipitation rate P and the amount of ^{10}Be accumulated scale with A_c/A_p. The inset in c)
695 shows the relation between $[^{10}Be]_{wet}$ and 1/P for the additive effect (neglecting dry and recycled ^{10}Be
696 components). Its y-intercept (YI, in at/m^3) is set by F_{prod}/C, i.e. the production flux of ^{10}Be and the water
697 condensation rate. This schematic plot is modified from Willenbring and von Blanckenburg (2010b).

698

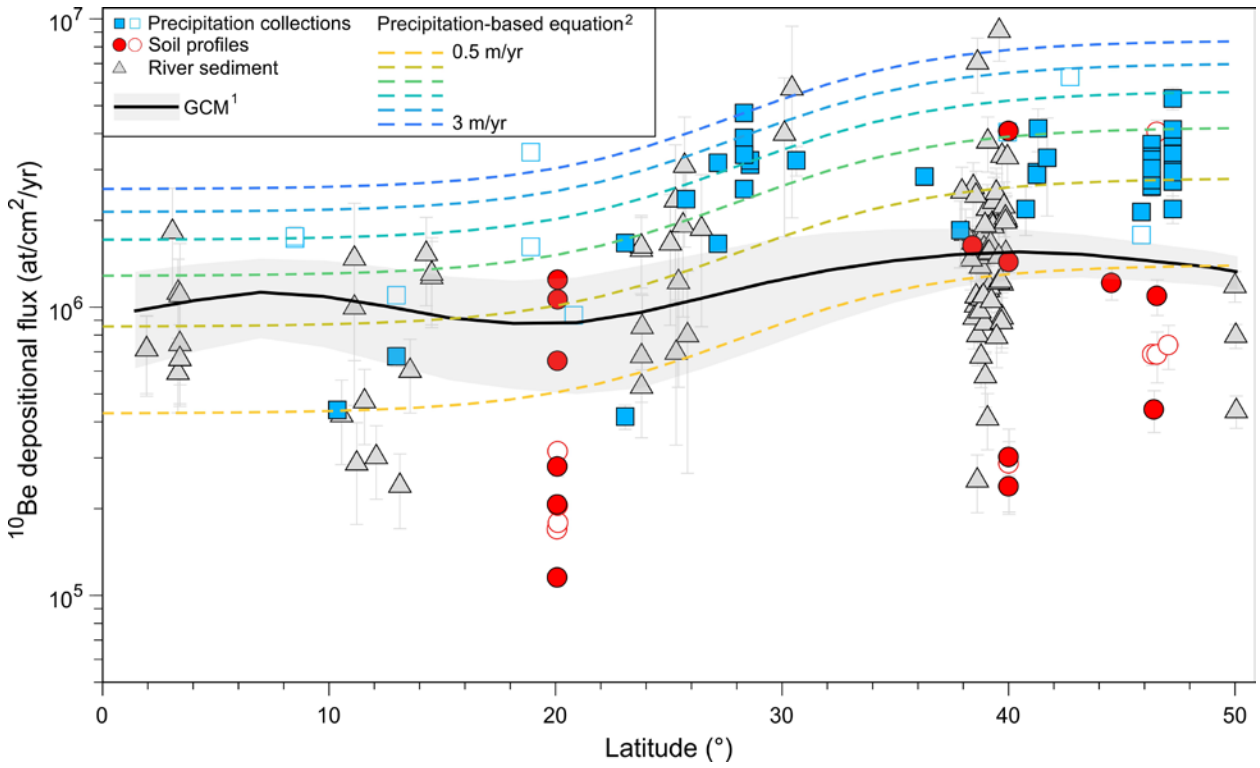

699

700 Fig. 4 Latitudinal distribution of measured and modeled ^{10}Be depositional fluxes derived from the
701 approaches compiled in this study. The latitude shown on the X-axis equally refers to the southern and
702 northern hemispheres, respectively. Note that the latitudes of river sediments are those of sampling
703 locations. 1) GCM results of the average Holocene ^{10}Be production and climatic conditions are sourced
704 from Heikkilä and von Blanckenburg (2015), and the average flux (black line) and the standard deviation
705 (gray shade) at each latitudinal zone are shown. 2) Results from precipitation-based fitting equation (Eq.
706 (5)) are from Graly et al. (2011). For comparison between different approaches, all flux data were
707 normalized to an average Holocene ^{10}Be production rate (see Fig. 2). For each dataset, only filled symbols
708 are considered representative and thus used for the discussion of fluxes, whereas flux data shown by open
709 symbols are considered potentially unrepresentative and only shown for completeness.

710

711

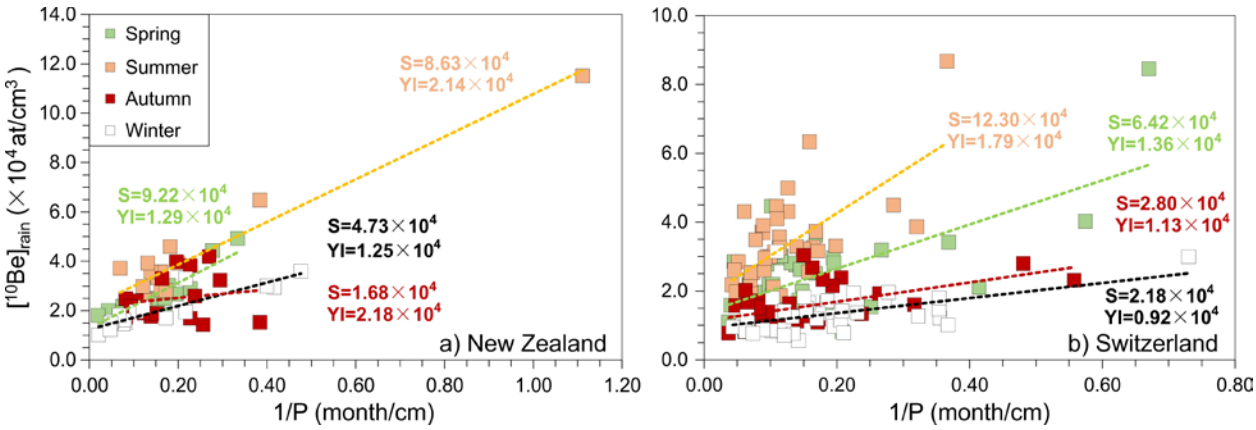

712

713 Fig. 5 Plot of the inverse of monthly precipitation rate (1/P) and $[^{10}Be]_{rain}$ in (a) New Zealand and (b)

714 Switzerland based on monthly records. The slope (S) and y-intercept (YI) are shown for each fit.

715

716

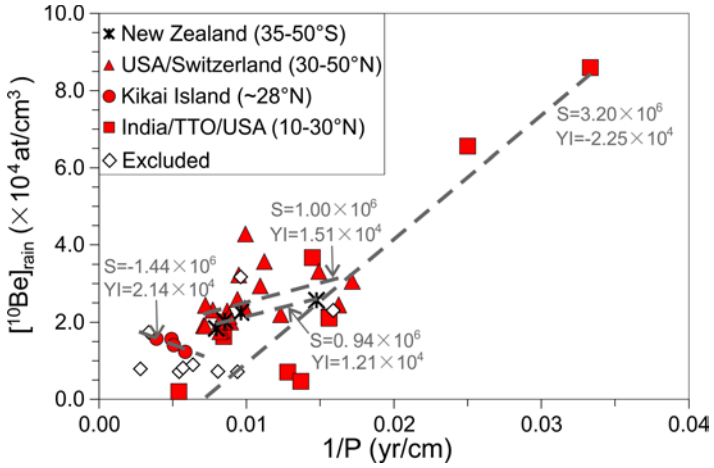

717

718 Fig. 6 Plot of inverse of annual precipitation rate (1/P) and mean $[^{10}Be]_{rain}$ based on annual records (data
719 in Supplementary dataset). The slope (S) and y-intercept (YI) are shown for each fit. Series
720 "India/TTO/USA (10-30° N)" includes precipitation data from India (majority), Trinidad (shortened as
721 TTO) and USA at 10-30° N. Note that data from northern India were excluded in a previous data
722 compilation (Graly et al., 2011) as they were assumed to be affected by significant but unquantified dust
723 ^{10}Be flux. In contrast, we still include such dataset here because recent modeling studies on global dust
724 distribution (Mahowald et al., 2005) show that the dust flux in northern India is not outstandingly high (5
725 to 20 g/m^2/yr). The records with a collection period of less than 9 months are considered unrepresentative
726 and marked as "Excluded" (open symbols). The uncertainties of $[^{10}Be]_{rain}$ are generally lower than the
727 symbol size.

728

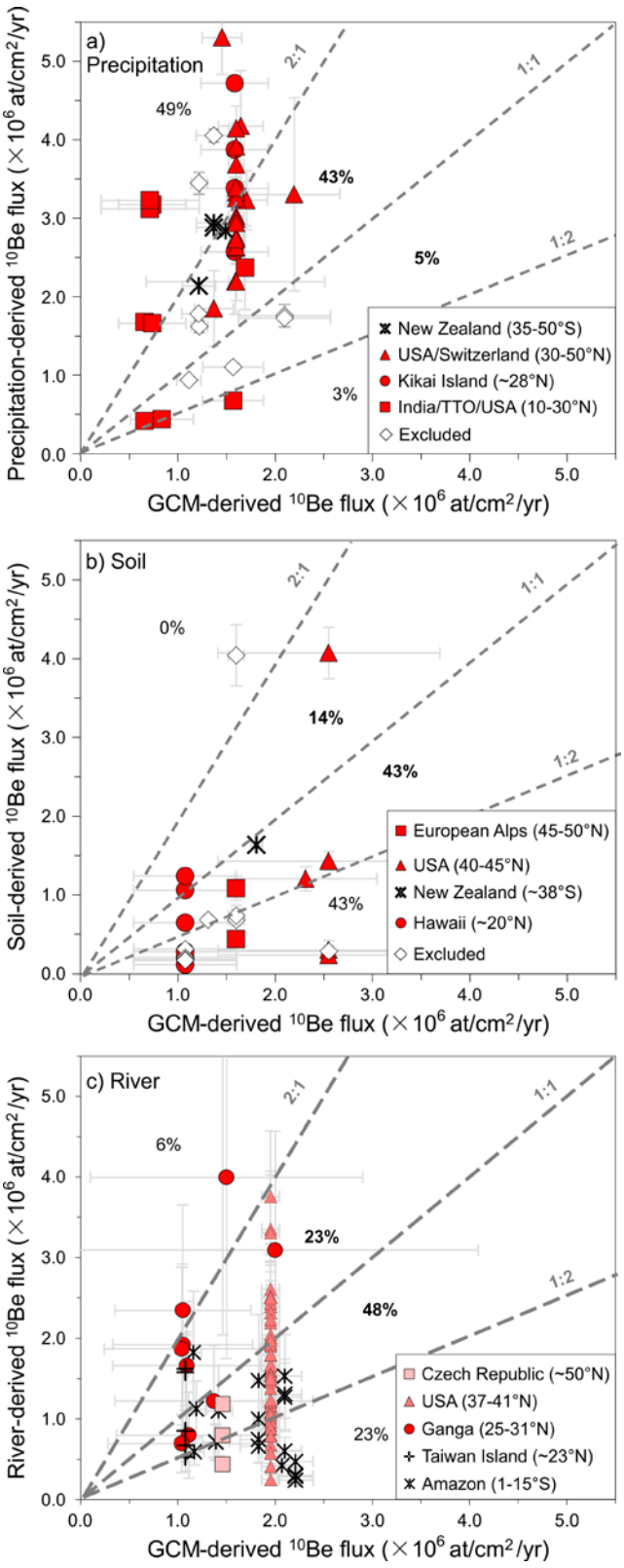
a)
Precipitation
49%
43%
5%
3%
2:1
1:1
1:2
New Zealand (35-50°S)
USA/Switzerland (30-50°N)
Kikai Island (~28°N)
India/TTO/USA (10-30°N)
Excluded
Precipitation-derived ¹⁰Be flux (×10⁶ at/cm²/yr)
GCM-derived ¹⁰Be flux (×10⁶ at/cm²/yr)
b) Soil
0%
14%
43%
43%
European Alps (45-50°N)
USA (40-45°N)
New Zealand (~38°S)
Hawaii (~20°N)
Excluded
Soil-derived ¹⁰Be flux (×10⁶ at/cm²/yr)
GCM-derived ¹⁰Be flux (×10⁶ at/cm²/yr)
c) River
6%
23%
48%
23%
Czech Republic (~50°N)
USA (37-41°N)
Ganga (25-31°N)
Taiwan Island (~23°N)
Amazon (1-15°S)
River-derived ¹⁰Be flux (×10⁶ at/cm²/yr)
GCM-derived ¹⁰Be flux (×10⁶ at/cm²/yr)

729

Fig. 7 Comparison between GCM-derived ^{10}Be depositional fluxes and precipitation- (a) or soil- (b) derived ^{10}Be depositional fluxes and between basin-averaged ^{10}Be depositional fluxes from GCM and riverine export ^{10}Be fluxes (c). Note that error bars of ^{10}Be fluxes can be smaller than the symbol size for some locations. The GCM-derived flux is based on the average Holocene model of ECHAM5-HAM (Heikkilä and von Blanckenburg, 2015). The corresponding flux uncertainty is the difference between modern and early Holocene model runs, or standard deviation among adjacent grid cell values (applicable for some riverine data, see details in Supplementary dataset). Precipitation- and soil- derived ^{10}Be flux data are normalized to an average Holocene production rate for comparison. The "Excluded" series in a) is the same as Fig. 6. "Excluded" series in b) includes profiles with significant erosional loss, incomplete sampling or high ^{10}Be inheritance (see details in Supplementary dataset). Only riverine fluxes derived from ^{10}Be (meteoric)/^{9}Be ratios are shown in (c). Three riverine flux data (range: $5.74\text{-}9.09 \times 10^6$ at/cm^2/yr) are out of the y-axis range and not shown in Fig. 7c, but they are included in the statistics. Each number in the figure represents the percentage of dataset falling in the corresponding domain (divided by the dashed lines).

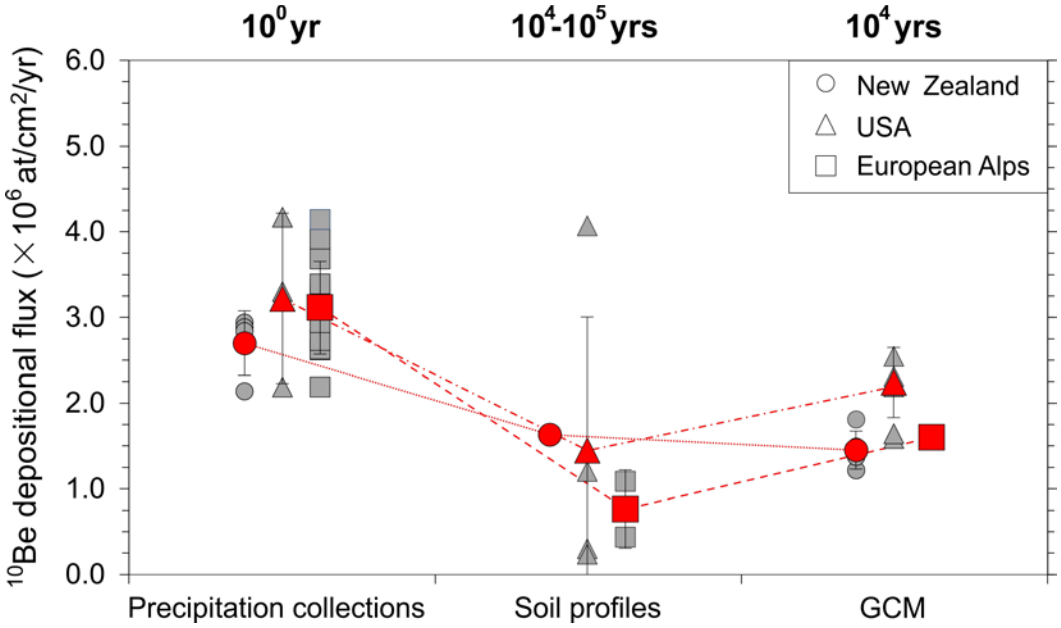

746

747 Fig. 8 Comparison of ^{10}Be depositional fluxes derived from three approaches across timescales. The gray
748 symbols are individual data, and the red symbols are average values derived thereof with an uncertainty
749 of one standard deviation. "Precipitation collections" and "Soil profiles" are measurements over
750 contemporary and millennial timescales, respectively. "GCM" is a modeled dataset derived from
751 ECHAM5-HAM output over average Holocene conditions (Heikkilä and von Blanckenburg, 2015). The
752 integration timescale of each method is provided at the top. All flux data are normalized to the average
753 Holocene ^{10}Be production rate. Dashed red lines connect mean values of every approach applied in the
754 same region.

755

Supplementary materials for Deng et al. (2020, EPSL)

1. Reconstruction of paleo-^{10}Be production rates

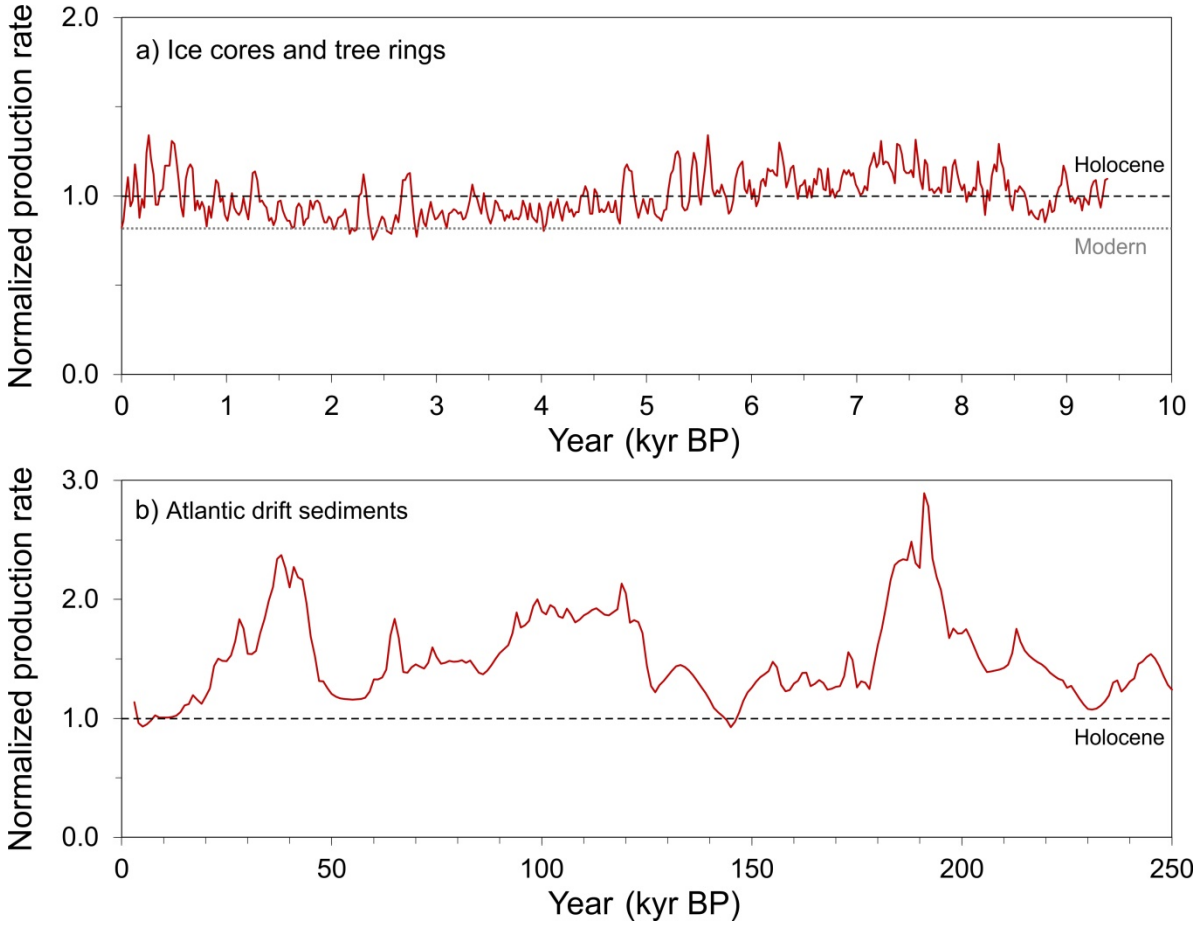

Fig. S1 Temporal variations of the global-averaged ^{10}Be production rates reconstructed from a) ice cores and tree rings in the Holocene (Steinhilber et al., 2012); b) highly accumulating Atlantic drift sediments since 250 ka (Christl et al., 2010). Each curve is normalized to its average production rate in the Holocene (see the black dashed line). Note that the average ^{10}Be production rate in the Holocene (a) is ~1.23 times that of the modern value (gray dot line). All ^{10}Be fluxes in this study are normalized to the average Holocene production rate by dividing by the average normalized production rates during the integration timescale of the archive, upon which the normalization will be done using either curve a) (e.g. for precipitation records) or b) (e.g. for soil profiles).

2. Estimation of recycled ^{10}Be flux

Table S1 Recycled ^{10}Be flux estimate in New Zealand, Switzerland and USA. The range is 1.10-3.28 × 10^5 at/cm^2/yr.

Region	Station	Recycled ^{10}Be	Total ^{10}Be depositional flux[3]	Recycled ^{10}Be flux	Data source
		%	at/cm^2/yr	at/cm^2/yr	
New Zealand	Gracefield	9.5%[1]	2.51E+06	2.38E+05	Graham et al. (2003)
New Zealand	Leigh	9.5%[1]	2.40E+06	2.28E+05	Graham et al. (2003)
New Zealand	Dunedin	16.1%[1]	1.81E+06	2.91E+05	Graham et al. (2003)
Switzerland	Dubendorf	7.5%[1]	2.31E+06	1.73E+05	Heikkilä et al. (2008)
Switzerland	Jungfraujoch	6.2%[1]	2.21E+06	1.37E+05	Heikkilä et al. (2008)
USA	Tacoma	8%[2]	3.58E+06	1.20E+05	Monaghan et al. (1986)
USA	Berkeley	21%[2]	1.25E+06	1.10E+05	Monaghan et al. (1986)
USA	Salt Lake City	29%[2]	1.47E+06	1.80E+05	Monaghan et al. (1986)
USA	College Station	26%[2]	2.17E+06	2.37E+05	Monaghan et al. (1986)
USA	Argonne	35%[2]	2.23E+06	3.28E+05	Monaghan et al. (1986)
USA	Miami	26%[2]	1.60E+06	1.75E+05	Monaghan et al. (1986)
USA	New Haven	20%[2]	2.82E+06	2.37E+05	Monaghan et al. (1986)

Note: 1. The percentage of recycled ^{10}Be is calculated using ^{10}Be/^{7}Be ratios by Graly et al. (2011).

2. The percentage of recycled ^{10}Be is calculated by multiplying ^{238}U-derived dust flux by assumed dust ^{10}Be concentration. However, in the original calculation, Monaghan et al. (1986) assumed an extremely high ^{10}Be concentration in dust (5×10^8 at/g) compared to recent observations (2.1×10^8 at/g on average) (Shen et al., 2010). Hence, we recalculated the recycled ^{10}Be% (shown here) using a dust ^{10}Be concentration of 2.1×10^8 at/g.

3. All the ^{10}Be data are normalized to the AMS standard KNSTD07 (Nishiizumi et al., 2007), but the correction for temporal variability in ^{10}Be production is not done here. We refer to Table SD1 in Supplementary Dataset for production-normalized fluxes.

References in Supplementary materials:

Christl, M., Lippold, J., Steinhilber, F., Bernsdorff, F., Mangini, A., 2010. Reconstruction of global 10 Be production over the past 250 ka from highly accumulating Atlantic drift sediments. Quat. Sci. Rev. 29, 2663-2672.

Graham, I., Ditchburn, R., Barry, B., 2003. Atmospheric deposition of 7Be and 10Be in New Zealand rain (1996-98). Geochim. Cosmochim. Acta 67, 361-373.

Graly, J.A., Reusser, L.J., Bierman, P.R., 2011. Short and long-term delivery rates of meteoric 10Be to terrestrial soils. Earth Planet. Sci. Lett. 302, 329-336.

Heikkilä, U., Beer, J., Alfimov, V., 2008. Beryllium-10 and beryllium-7 in precipitation in Dübendorf (440 m) and at Jungfraujoch (3580 m), Switzerland (1998-2005). Journal of Geophysical Research Atmospheres 113, 1-10.

Monaghan, M.C., Krishnaswami, S., Turekian, K.K., 1986. The global-average production rate of 10 Be. Earth Planet. Sci. Lett. 76, 279-287.

Nishiizumi, K., Imamura, M., Caffee, M.W., Southon, J.R., Finkel, R.C., McAninch, J., 2007. Absolute calibration of 10Be AMS standards. Nucl. Instrum. Methods Phys. Res., Sect. B 258, 403-413.

Shen, C., Beer, J., Kubik, P., Sun, W., Liu, T., Liu, K., 2010. 10Be in desert sands, falling dust and loess in China. Nucl. Instrum. Methods Phys. Res., Sect. B 268, 1050-1053.

Steinhilber, F., Abreu, J.A., Beer, J., Brunner, I., Christl, M., Fischer, H., Heikkilä, U., Kubik, P.W., Mann, M., McCracken, K.G., Miller, H., Miyahara, H., Oerter, H., Wilhelms, F., 2012. 9,400 years of cosmic radiation and solar activity from ice cores and tree rings. Proceedings of the National Academy of Sciences 109, 5967-5971.

Table SD1 Compiled ^{10}Be depositional flux data from precipitation collections and the correspon

Station[1]	Country/region	Lat.[2]	Lon.	Observation time span	
		°N	°E	Start time	End time
New Zealand (35-50°S)					
Dunedin (1997)	New Zealand	-45,867	170,500	01.10.1997	1998/9/30
Gracefield (1996)	New Zealand	-41,250	174,917	01.10.1996	30.09.1997
Gracefield (1997)	New Zealand	-41,250	174,917	01.10.1997	30.09.1998
Leigh	New Zealand	-36,283	174,800	01.10.1997	30.09.1998
India, etc (10-30°N)					
Trinidadian	Trinidad	10,361	-61,250	1987	1988
Bangalore(1980)	India	12,967	77,583	01.07.1980	15.06.1981
Ahmedabad (1980)	India	23,067	72,633	15.06.1980	04.07.1981
Ahmedabad (1979)	India	23,067	72,633	22.06.1979	14.06.1980
Miami	USA	25,757	-80,197	01.08.1980	01.08.1981
Agra (1980)	India	27,167	78,033	25.06.1980	03.07.1981
Agra (1979)	India	27,167	78,033	04.07.1979	22.06.1980
Delhi (1980)	India	28,583	77,200	20.06.1980	10.07.1981
Delhi (1979)	India	28,583	77,200	14.06.1979	19.06.1980
Kikai Island (~28°N)					
Site.2 (2000)	Kikai island	28,319	129,985	05.06.2000	24.06.2001
Site.2 (2001)	Kikai island	28,319	129,985	24.06.2001	29.06.2002
Site 1 (2000)	Kikai island	28,324	129,928	05.06.2000	24.06.2001
Site 1 (2001)	Kikai island	28,324	129,928	25.06.2001	29.06.2002
USA/Switzerland (30-50°N)					
College Station	USA	30,628	-96,335	17.10.1980	09.11.1981
Berkeley	USA	37,871	-122,273	10.12.1980	15.12.1981
Salt Lake City	USA	40,760	-111,892	04.12.1980	04.12.1981
New Haven	USA	41,304	-72,929	24.12.1980	07.01.1982
Argonne	USA	41,706	-87,982	15.09.1980	15.09.1981
Jungfraujoch (1998)	Switzerland	46,320	7,590	01.01.1998	31.12.1998
Jungfraujoch (1999)	Switzerland	46,320	7,590	01.01.1999	31.12.1999
Jungfraujoch (2000)	Switzerland	46,320	7,590	01.01.2000	31.12.2000
Jungfraujoch (2001)	Switzerland	46,320	7,590	01.01.2001	31.12.2001
Jungfraujoch (2002)	Switzerland	46,320	7,590	01.01.2002	31.12.2002
Jungfraujoch (2003)	Switzerland	46,320	7,590	01.01.2003	31.12.2003
Jungfraujoch (2004)	Switzerland	46,320	7,590	01.01.2004	31.12.2004
Tacoma	USA	47,248	-122,444	09.08.1980	03.08.1981
Dubendorf (1998)	Switzerland	47,250	8,270	01.01.1998	31.12.1998
Dubendorf (1999)	Switzerland	47,250	8,270	01.01.1999	31.12.1999
Dubendorf (2000)	Switzerland	47,250	8,270	01.01.2000	31.12.2000
Dubendorf (2001)	Switzerland	47,250	8,270	01.01.2001	31.12.2001
Dubendorf (2002)	Switzerland	47,250	8,270	01.01.2002	31.12.2002
Dubendorf (2003)	Switzerland	47,250	8,270	01.01.2003	31.12.2003
Dubendorf (2004)	Switzerland	47,250	8,270	01.01.2004	31.12.2004
Below are stations with observation period <9 months					
Dunedin(1997)	New Zealand	-45,867	170,500	01.03.1997	30.09.1997
Hokitika	New Zealand	-42,717	170,967	01.08.1998	30.11.1998
Kaitoke	New Zealand	-39,959	175,089	01.01.1997	31.05.1997
Trivandrium(1980)	India	8,483	76,950	01.04.1980	15.08.1980

Trivandrium(1979)	India	8,483	76,950	09.07.1979	14.11.1979
Bangalore(1979)	India	12,967	77,583	25.06.1979	19.10.1979
Bombay	India	18,900	72,817	20.06.1979	21.11.1979
Khandala	India	18,900	73,917	23.06.1979	11.08.1979
Cuttack	India	20,800	85,933	21.06.1979	04.11.1979

Note: 1. Stations are sorted and grouped based on latitude. Observations of multiple years at the s
2. When coordinates are not provided in the original study (e.g. USA & Trinidad), we estimate La
3. Observation period is estimated based on the starting time and end time of sample collection. S
4. The ^{10}Be concentrations used for flux calculation have been normalized to the same AMS stan
5. The average solar modulation factor (ϕ) during sample collection period is sourced from www.
6. All flux data are normalized to a modern ϕ of 501.76 MeV, using the modelled relationship bet
7. ϕ-normalized $[^{10}Be]_{rain}$ is used in Fig. 6.
8. The ϕ-normalized flux was further normalized to the average Holocene ^{10}Be production rate, i.
9. The fluxes are calculated based on Eq. (5) in the main text and then normalized to the average
10. GCM-derived fluxes for the average Holocene climate conditions are from Heikkilä and von

ıding modelled flux

Observation period[3]	Precipitation rate	Depositional flux[4]	1 sigma	AMS standard-normalized $[^{10}Be]_{rain}$	1 sigma
day	cm/yr	at/cm^2/yr	at/cm^2/yr	at/cm^3	at/cm^3
365	68	1,81E+06	9,13E+03	2,67E+04	1,35E+02
365	117	2,57E+06	9,13E+03	2,20E+04	7,79E+01
365	104	2,44E+06	9,13E+03	2,35E+04	8,80E+01
365	126	2,40E+06	1,83E+04	1,91E+04	1,45E+02
730	184	3,60E+05	0,00E+00	1,95E+03	0,00E+00
350	78	4,56E+05	3,65E+04	5,85E+03	4,68E+02
385	73	2,83E+05	2,74E+04	3,87E+03	3,75E+02
359	64	1,22E+06	6,39E+04	1,91E+04	9,98E+02
366	118	1,60E+06	3,62E+05	1,35E+04	3,06E+03
374	64	1,12E+06	2,74E+04	1,75E+04	4,28E+02
355	30	2,32E+06	9,12E+04	7,72E+04	3,04E+03
386	69	2,11E+06	6,39E+04	3,05E+04	9,26E+02
372	40	2,35E+06	7,30E+04	5,88E+04	1,82E+03
385	253	3,20E+06	6,94E+04	1,26E+04	2,74E+02
371	202	2,70E+06	5,46E+04	1,34E+04	2,71E+02
385	195	2,29E+06	9,49E+04	1,17E+04	4,86E+02
370	170	1,79E+06	3,98E+04	1,06E+04	2,34E+02
389	115	2,17E+06	2,53E+05	1,89E+04	2,21E+03
371	61	1,25E+06	3,26E+05	2,03E+04	5,29E+03
366	58	1,47E+06	2,80E+05	2,53E+04	4,81E+03
380	105	2,82E+06	4,79E+05	2,68E+04	4,55E+03
366	91	2,23E+06	8,32E+05	2,44E+04	9,10E+03
365	120	2,20E+06	1,73E+05	1,83E+04	1,44E+03
365	122	2,05E+06	1,73E+05	1,68E+04	1,42E+03
305	129	2,49E+06	1,73E+05	1,92E+04	1,33E+03
335	141	2,33E+06	1,73E+05	1,65E+04	1,22E+03
365	139	2,23E+06	1,73E+05	1,61E+04	1,24E+03
365	112	1,87E+06	1,73E+05	1,67E+04	1,54E+03
365	122	2,30E+06	1,73E+05	1,89E+04	1,42E+03
360	100	3,58E+06	3,16E+05	3,56E+04	3,15E+03
335	81	1,84E+06	2,01E+05	2,27E+04	2,49E+03
305	106	2,65E+06	2,01E+05	2,49E+04	1,89E+03
365	89	2,65E+06	2,01E+05	2,97E+04	2,26E+03
365	138	2,90E+06	2,01E+05	2,10E+04	1,46E+03
365	113	2,05E+06	2,01E+05	1,82E+04	1,78E+03
365	67	1,85E+06	2,01E+05	2,76E+04	3,01E+03
335	101	2,22E+06	2,01E+05	2,20E+04	1,99E+03
214	63	1,57E+06	9,13E+03	2,50E+04	1,45E+02
122	295	5,24E+06	2,74E+04	1,78E+04	9,28E+01
151	104	3,57E+06	7,30E+04	3,43E+04	7,02E+02
137	157	1,23E+06	2,74E+04	7,85E+03	1,74E+02

129	175	1,25E+06	1,00E+05	7,14E+03	5,74E+02
117	124	7,85E+05	3,65E+04	6,33E+03	2,94E+02
155	184	1,16E+06	5,47E+04	6,30E+03	2,98E+02
50	355	2,49E+06	1,00E+05	7,02E+03	2,83E+02
137	106	6,66E+05	2,74E+04	6,26E+03	2,57E+02

ame station are separated and the starting time (year) is added behind the station name
at. & Lon. from Google Earth.
amples with observation period< 9 months are not used for statistical analysis in this study.
dard KNSTD07.
.faa.gov/data_research/research/med_humanfacs/aeromedical/ radiobiology/heliocentric/
tween ϕ and global-averaged production rate (Masarik and Beer, 2009) as calculated for modern condition

e. multiplied by a factor of ~1.23 according to Steinhilber et al. (2012).
Holocene ^{10}Be production rates.
Blanckenburg (2015). The dataset is rescaled to an average Holocene production rate.

Average ϕ[5]	**ϕ-normalized flux**[6]	**1 sigma**	**ϕ-normalized $[^{10}Be]_{rain}$**[7]	**1 sigma**
MeV	at/cm^2/yr	at/cm^2/yr	at/cm^3	at/cm^3
429	1,74E+06	8,77E+03	2,56E+04	1,30E+02
369	2,39E+06	8,46E+03	2,04E+04	7,22E+01
429	2,34E+06	8,77E+03	2,26E+04	8,45E+01
429	2,31E+06	1,75E+04	1,84E+04	1,40E+02
488	3,57E+05	\	1,94E+03	\
907	5,48E+05	4,38E+04	7,02E+03	5,62E+02
901	3,39E+05	3,28E+04	4,64E+03	4,49E+02
719	1,36E+06	7,10E+04	2,12E+04	1,11E+03
911	1,92E+06	4,35E+05	1,63E+04	3,68E+03
907	1,35E+06	3,29E+04	2,11E+04	5,14E+02
719	2,58E+06	1,01E+05	8,59E+04	3,38E+03
907	2,53E+06	7,67E+04	3,67E+04	1,11E+03
721	2,62E+06	8,13E+04	6,55E+04	2,03E+03
904	3,83E+06	8,32E+04	1,51E+04	3,29E+02
830	3,14E+06	6,36E+04	1,56E+04	3,16E+02
904	2,75E+06	1,14E+05	1,41E+04	5,82E+02
830	2,09E+06	4,64E+04	1,23E+04	2,73E+02
924	2,62E+06	3,06E+05	2,28E+04	2,67E+03
913	1,50E+06	3,92E+05	2,44E+04	6,37E+03
921	1,78E+06	3,38E+05	3,05E+04	5,81E+03
909	3,39E+06	5,76E+05	3,22E+04	5,46E+03
909	2,68E+06	1,00E+06	2,93E+04	1,09E+04
446	2,13E+06	1,67E+05	1,78E+04	1,40E+03
578	2,14E+06	1,80E+05	1,75E+04	1,47E+03
909	2,99E+06	2,07E+05	2,31E+04	1,60E+03
819	2,70E+06	2,00E+05	1,91E+04	1,42E+03
868	2,64E+06	2,04E+05	1,90E+04	1,47E+03
903	2,24E+06	2,07E+05	2,00E+04	1,85E+03
637	2,46E+06	1,85E+05	2,02E+04	1,52E+03
911	4,31E+06	3,81E+05	4,29E+04	3,79E+03
446	1,78E+06	1,95E+05	2,20E+04	2,41E+03
578	2,75E+06	2,10E+05	2,59E+04	1,97E+03
909	3,18E+06	2,42E+05	3,57E+04	2,71E+03
819	3,36E+06	2,34E+05	2,43E+04	1,69E+03
868	2,43E+06	2,38E+05	2,15E+04	2,11E+03
903	2,22E+06	2,41E+05	3,31E+04	3,60E+03
642	2,39E+06	2,16E+05	2,36E+04	2,14E+03
360	1,45E+06	8,42E+03	2,30E+04	1,34E+02
459	5,12E+06	2,68E+04	1,74E+04	9,07E+01
360	3,29E+06	6,73E+04	3,16E+04	6,47E+02
774	1,40E+06	3,12E+04	8,94E+03	1,99E+02

781	1,43E+06	1,15E+05	8,16E+03	6,55E+02
781	8,96E+05	4,17E+04	7,23E+03	3,36E+02
768	1,32E+06	6,22E+04	7,15E+03	3,38E+02
742	2,80E+06	1,13E+05	7,88E+03	3,18E+02
781	7,61E+05	3,13E+04	7,15E+03	2,94E+02

ıs (Heikkilä et al., 2013b).

Production-normalized flux[8]	**1 sigma**	**Precipitation data fitting-based ^{10}Be flux**[9]	**GCM-derived flux (average Holocene)**[10]	**1 sigma**
at/cm^2/yr	at/cm^2/yr	at/cm^2/yr	at/cm^2/yr	at/cm^2/yr
2,14E+06	1,08E+04	1,86E+06	1,22E+06	1,70E+05
2,94E+06	1,04E+04	3,11E+06	1,37E+06	1,80E+05
2,88E+06	1,08E+04	2,75E+06	1,37E+06	1,80E+05
2,84E+06	2,16E+04	3,00E+06	1,49E+06	1,80E+05
4,40E+05 \		1,61E+06	8,35E+05	3,24E+05
6,75E+05	5,40E+04	6,93E+05	1,57E+06	3,14E+05
4,17E+05	4,04E+04	8,36E+05	6,55E+05	3,22E+04
1,67E+06	8,75E+04	7,33E+05	6,55E+05	3,22E+04
2,37E+06	5,36E+05	1,57E+06	1,69E+06	3,14E+03
1,66E+06	4,05E+04	9,33E+05	7,36E+05	3,44E+05
3,17E+06	1,25E+05	4,37E+05	7,36E+05	3,44E+05
3,12E+06	9,44E+04	1,10E+06	7,14E+05	5,04E+05
3,23E+06	1,00E+05	6,40E+05	7,14E+05	5,04E+05
4,72E+06	1,02E+05	3,98E+06	1,58E+06	3,45E+05
3,87E+06	7,84E+04	3,17E+06	1,58E+06	3,45E+05
3,38E+06	1,40E+05	3,07E+06	1,58E+06	3,45E+05
2,57E+06	5,71E+04	2,67E+06	1,58E+06	3,45E+05
3,23E+06	3,77E+05	2,09E+06	1,71E+06	2,12E+05
1,85E+06	4,82E+05	1,53E+06	1,37E+06	1,99E+05
2,19E+06	4,17E+05	1,53E+06	1,59E+06	9,20E+05
4,17E+06	7,09E+05	2,80E+06	1,65E+06	2,30E+05
3,30E+06	1,23E+06	2,44E+06	2,20E+06	4,70E+05
2,62E+06	2,06E+05	3,31E+06	1,60E+06	8,00E+04
2,63E+06	2,21E+05	3,36E+06	1,60E+06	8,00E+04
3,68E+06	2,55E+05	3,57E+06	1,60E+06	8,00E+04
3,33E+06	2,47E+05	3,89E+06	1,60E+06	8,00E+04
3,25E+06	2,51E+05	3,83E+06	1,60E+06	8,00E+04
2,76E+06	2,55E+05	3,09E+06	1,60E+06	8,00E+04
3,03E+06	2,28E+05	3,36E+06	1,60E+06	8,00E+04
5,30E+06	4,69E+05	2,78E+06	1,45E+06	2,03E+05
2,19E+06	2,40E+05	2,24E+06	1,60E+06	7,88E+04
3,39E+06	2,58E+05	2,95E+06	1,60E+06	7,88E+04
3,91E+06	2,98E+05	2,47E+06	1,60E+06	7,88E+04
4,14E+06	2,88E+05	3,83E+06	1,60E+06	7,88E+04
2,99E+06	2,93E+05	3,13E+06	1,60E+06	7,88E+04
2,73E+06	2,97E+05	1,86E+06	1,60E+06	7,88E+04
2,94E+06	2,66E+05	2,80E+06	1,60E+06	7,88E+04
1,78E+06	1,04E+04	1,73E+06	1,21E+06	1,75E+05
6,30E+06	3,30E+04	7,95E+06	1,26E+06	2,25E+05
4,05E+06	8,29E+04	2,71E+06	1,37E+06	1,81E+05
1,73E+06	3,84E+04	1,36E+06	2,10E+06	4,73E+05

1,76E+06	1,41E+05	1,52E+06	2,10E+06	4,73E+05
1,10E+06	5,13E+04	1,10E+06	1,57E+06	3,12E+05
1,62E+06	7,66E+04	1,80E+06	1,22E+06	8,40E+04
3,45E+06	1,39E+05	3,47E+06	1,22E+06	8,40E+04
9,37E+05	3,85E+04	1,11E+06	1,11E+06	1,24E+05

Reference

Graham et al. (2003)
Graham et al. (2003)
Graham et al. (2003)
Graham et al. (2003)

Brown et al. (1992)
Somayajulu et al. (1984)
Somayajulu et al. (1984)
Somayajulu et al. (1984)
Monaghan et al. (1986)
Somayajulu et al. (1984)
Somayajulu et al. (1984)
Somayajulu et al. (1984)
Somayajulu et al. (1984)

Maejima et al. (2005)
Maejima et al. (2005)
Maejima et al. (2005)
Maejima et al. (2005)

Monaghan et al. (1986)
Monaghan et al. (1986)
Monaghan et al. (1986)
Monaghan et al. (1986)
Monaghan et al. (1986)
Heikkila et al. (2008a)
Heikkila et al. (2008a)
Heikkila et al. (2008a)
Heikkila et al. (2008a)
Heikkila et al. (2008a)
Heikkila et al. (2008a)
Heikkila et al. (2008a)
Monaghan et al. (1986)
Heikkila et al. (2008a)
Heikkila et al. (2008a)
Heikkila et al. (2008a)
Heikkila et al. (2008a)
Heikkila et al. (2008a)
Heikkila et al. (2008a)
Heikkila et al. (2008a)

Graham et al. (2003)
Graham et al. (2003)
Graham et al. (2003)
Somayajulu et al. (1984)

Somayajulu et al. (1984)
Somayajulu et al. (1984)
Somayajulu et al. (1984)
Somayajulu et al. (1984)
Somayajulu et al. (1984)